学位論文

生塩研一

Current Oscillations and Domain Instability in Semiconductors

Ken-ichi OSHIO

Department of Materials Science, Faculty of Science

Hiroshima University, Higashi-Hiroshima 739

March 1996

Abstract

Semiconductors are typical nonlinear systems which are suitable for understanding nonlinear dynamics because their dynamical variables such as electrical currents and fields can be measured very accurately and the experiments on them can be performed under precisely controlled conditions. Recently a variety of self-organization and pattern formation in semiconductors have attracted considerable attention and have been studied by many researchers.

In this thesis we treat three types of mechanisms in semiconductors which give rise to current oscillations due to the domain instabilities under strong excitation conditions. We present the models for these systems and give the results of our numerical simulations on them.

First, we give the results on the Gunn-effect device subject to the dc and the rf alternating fields which is an extension of a periodically driven nonlinear oscillator with no spatial degrees of freedom. Next, we discuss the behavior of the Gunn-effect device with the impact ionization in which electron-hole pairs are generated due to conduction electrons accelerated by the high-electric field. Actually, its possibility has been pointed out by some experimental evidence. Third, we present a one-dimensional system of Au-doped n-Ge in which the recombination instability leads the system to instability and current oscillations.

We describe the system using the partial differential equations and pursue its spatio-temporal behavior by the finite-difference method. In general, three types of modes of operation, the Ohmic, the quenched, and the transit-time modes, are found, and are classified on the basis of spatio-temporal behavior of the system. Non-periodic oscillations are also found in the transition region between the quenched and the transit-time modes. Their origins are clarified from spatio-temporal evolution of the high-field domain.

Acknowledgements

The author owes a debt of gratitude to Professor Kyoji Nishikawa for his constant support and encouragement during the preparation of this dissertation.

The author would like to express my deepest gratitude to Professor Hideo Yahata, who has suggested the field of research of the present thesis and given him constant and generous guidance with great patience in promoting this work.

Doctor Kanya Kusano and Doctor Hiroyuki Mori have taken an interest in my work and made many useful comments. The author greatly appreciated their generous advice in this matter.

Acknowledgement must also be made to Mr. Yoshio Suzuki and Mr. Minoru Hamada for their excellent cooperation.

Finally, the author wishes to express his sincere thanks to all members of *Nishikawa research group, Hiroshima University.*

Contents

1 Introduction **1**

1.1 Negative Differential Conductivity (NDC) 2

1.2 Gunn effect 3

1.3 Gunn effect with impact ionization 6

1.4 Recombination instability 7

1.5 Chaos in semiconductors 8

1.6 Composition of following chapters 9

2 Chaotic current oscillations in the Gunn-effect device under the dc and the rf bias voltages **13**

2.1 Introduction 13

2.2 Equations of motion and the method of solution 14

2.3 The motion under the dc bias voltage 18

2.4 The motion under the dc and rf bias voltage 20

2.4.1 Quasi-periodic behavior 21

2.4.2 Period-doubling cascade 21

3 Non-periodic current oscillations in the Gunn-effect device with the impact-ionization effect **33**

3.1 Introduction 33

3.2 Equations of motion and the method of solution 34

3.3 Simulational results 38

3.3.1 Case for low $\Phi_{\rm dc}$ 39

3.3.2 Case for high $\Phi_{\rm dc}$ 40

4 Current oscillations induced by recombination instability in semiconductors 49

4.1 Introduction 49

4.2 Equations of motion and simulation method 49

4.3 Simulational results 54

4.3.1 Fundamental motions 54

4.3.2 Peculiar motions 56

5 Summary and conclusion 71

Chapter 1

Introduction

A startling development on the understanding of the instabilities in semiconductors have been initiated by the invention of the transistor in 1940s. Semiconductors under sufficiently strong excitation conditions exhibit nonlinear transport properties such as deviation from linear ("Ohmic") current-voltage relations and instabilities leading to current oscillations associated with domain or filament formations. These instabilities are observed widely in a variety of materials and under different excitation conditions, and are considered to occur due to diverse physical mechanisms [1], and further they have been applied to various kinds of semiconductor devices.

In the last decades a remarkable progress has been made in our understanding of spatio-temporal evolution of nonlinear systems which appear in many different fields. Semiconductors are considered to be typical of these nonlinear systems. They are suitable for understanding the nonlinear dynamics because electrical currents, fields, and so on can be measured very accurately and the experiments can be performed under precisely controlled conditions. Recently a variety of self-organization and pattern formation in semiconductors have attracted considerable attention and have been studied by many researchers [2].

1.1 Negative Differential Conductivity (NDC)

The electrical instability under strong excitation in semiconductors is mostly caused by the nonlinearity such as negative differential conductivity (NDC) which is a regime where the current density j decreases with the electric field E, that is, the negative gradient of the $j-E$ curve ($\mathrm{d}j/\mathrm{d}E < 0$). NDC brings the homogeneous steady state to be unstable, and a spatial fluctuation of the electric field or current can lead to a splitting of the system into regions having different electrical properties from each other [3].

NDC can be divided into two classes, *i.e.*, a voltage-controlled NDC and a current-controlled NDC which are called as N-shaped NDC (NNDC) and S-shaped NDC (SNDC) according to the shape of the $j-E$ curve, respectively [1]. As for NNDC the high-electric-field domain (for simplicity, we call this simply "the domain" below) is formed perpendicularly to the bias direction. The domain is also called the dipole domain in that it consists of an electron accumulation layer preceded by a depletion layer. The domain is usually formed near the electrode and propagates toward another electrode suffering the voltage imposed on the device (Fig. 1.1(a) and Fig. 1.2(a)). The Gunn-effect device(Gunn diode) and Esaki diode are related to NNDC, and are frequently used as microwave generators. The instabilities associated with NNDC are also called the domain electrical instability in that the system leads to the state where formation and propagation of the domain occur. It has been studied in detail especially in the 1960s and 1970s, and has attracted much attention from both pure and applied points of view [4]. As for SNDC the high-current-density filament (for simplicity, we call this simply "the filament" below) is formed running along the bias direction (Fig. 1.1(b) and Fig. 1.2(b)). Thyristors, pnpn diodes, and pin diodes are related to SNDC, and are used frequently as electronic switches.

NDC is caused either by junction(metal-semiconductor) effects or bulk effects [3]. Esaki diode and pnpn diodes are associated with junction effects. The NDC mechanisms based upon bulk effects can be classified to four groups, *i.e.*, the drift instability, the g-r instability, the electron-overheating instability, and the electrothermal instability which are associated with the nonlinearity on the local electric field of the mobility, the carrier density, the electron temperature, and the lattice temperature, respectively [1].

In this thesis we deal with the domain instability associated with NNDC and bulk effects of devices. As concrete systems to investigate these dynamics we selected the Gunn-effect device associated with the drift instability and the gold-doped n-Ge associated with the recombination instability which is one of the g-r instabilities.

1.2 Gunn effect

First, we review briefly the works related to the Gunn-effect. In 1958 Krömer proposed the negative-mass amplifier theory for NDC based on a negative effective mass originated from the energy band structure for p-Ge crystal [5]. However, his principle had the difficulty in finding a means to make a sufficiently large portion of carriers have a negative mass. A few years later, Ridley and Watkins suggested the possibility of negative resistance effects using other band structure properties such as those in the III-V compounds and Ge-Si alloys [6]. Hilsum also gave a similar analysis of conduction in two bands, and he stated the possibilities of obtaining a band structure suitable for NDC by GaSb and semi-insulating GaAs [7].

The Gunn-effect device such as n-GaAs generates periodic current oscillations at microwave frequencies when the imposed bias field exceeds a threshold value of a few kV/cm. This phenomenon was first discovered experimentally by Gunn in 1963 [8,9], and it has been called the Gunn effect. Krömer [10] showed that all of the known properties of the Gunn effect were consistent with the "two-valley" model independently proposed by Ridley and Watkins and by Hilsum as follows. This effect occurs as a result of cyclic propagation of the high-electric-field domain nucleating at the cathode and vanishing at the anode. The reason for formation and subsequent persistence of the domain is that the carrier exhibits a negative differential mobility(NDM) implying a decrease in drift velocity with increase in the field over the range of the electric field above a threshold and that the field imposed on the system is maintained to be high enough to satisfy the NDM condition. The mechanism for the NDM is attributed to the transferred-electron effect which is a field-induced transfer of carriers from a low-lying high-mobility valley to high-lying low-mobility satellite valleys in the momentum space. The Gunn-effect device

is voltage-controlled and thus characterized by NNDC. This gives the possibility for sustaining an NDM-governed high-field domain together with the Ohmic low-field domain in the system as the field can be multivalued for the same value of the current. The convincing evidence that this mechanism is responsible for the Gunn effect, was shown experimentally by Hutson *et al.*, by decreasing the energy separation between the valley minima by means of hydrostatic pressure [11]. In addition to experiments, device simulation on a digital computer has been a quite useful tool to elucidate mechanism underlying those highly nonlinear transport phenomena which are associated with the complicated spatial structure such as the domain [12-30,79,80].

McCumber and Chynoweth [12] reported a confirmation of the two-valley model and showed numerically that it satisfactorily accounts for the high-frequency amplification and oscillation phenomena, by assuming that the electrons are Boltzmann-distributed with a common temperature, and possess a common thermal relaxation time, and that the dynamics is governed by Poisson's equation, the electron continuity equation, the energy transport equation, and an equation expressing the average electron velocity in terms of the electric field and diffusion.

Krömer [13] presented a semi-phenomenological study using numerical simulations for a Gunn-effect device to obtain a detailed understanding of the domain dynamics. Although McCumber and Chynoweth used Maxwell-Boltzmann statistics to represent the energy distribution for carriers, he took a more simple formula for $v-E$ characteristics containing empirical parameters, where v is the average drift velocity for electrons and E is the local electric field. He investigated the influence on the current oscillation of the spatial nonuniformities such as noise fluctuations, local field concentrations at the source electrode interface due to interface irregularities, and so on. He found that when the bias voltage is suddenly applied, the field in the device with random doping fluctuations breaks into multiple-domains, and after the last domain has reached the anode, only one domain is normally formed during the following cycle since the electric field throughout the GaAs can now only rise at a slow rate. This behavior has been confirmed experimentally by Thim and Barber [31].

Thim [14] performed computer simulations for a bulk GaAs diode in a resonant circuit (which is different from the case of Krömer who used the dc bias voltage) in order to

investigate the influence of one-dimensional random doping fluctuations and localized inhomogeneities on the performance of bulk GaAs oscillators.

Various properties associated with metal-semiconductor contacts have attracted much attention and have been investigated by many researchers [34-38]. Contact characteristics are very important for understanding of the domain nucleating mechanism, and an appropriate model which represents the contact properties is required to pursue numerically the spatio-temporal evolution of the system. Grubin *et al.* [15] regarded the boundary conditions imposed on the device as the primary determinant of the electrical instability. They demonstrated numerically that the cathode depletion-layer solutions (Gunn found that a stationary cathode potential drop appeared in n-GaAs samples [32]) become unstable as the current approaches a critical value determined by the electric field at the cathode boundary using a fixed cathode boundary field model and a piecewise linear $v-E$ characteristics. Solomon *et al.* [17] showed an agreement between the experimental results and the model in which the sample is assumed to have an assigned value for the electric field at the cathode boundary, and stated that a good agreement between theory and experiment allows us to use the results of the model to determine important material characteristics. Such measurements have been made as a function of temperature and magnetic field. However, as also pointed out by themselves, their model has a difficulty in including the effect of avalanching within high-field domains. The possibility of the avalanching has been reported through experimental investigations by several authors [16,32,33,46].

Lakshminarayana and Partain [18] presented a simple and improved numerical scheme based on a first principle model for the simulation of Gunn-devices, and their scheme was found to be stable and efficient, and to accurately predict various large-signal dynamic properties of Gunn devices, using the implicit method and $n^+ - n - n^+$ sandwich device configuration which reflects the real device configuration, where n^+ and n are the high-doping and the low doping regions respectively (cf. Fig. 2.2). As a treatment of the contact, various types of notches which mean the reduction of the doping density over a short region, were introduced adjacent to the cathode. It was not intended that these notches should quantitatively describe localized crystal damage, interfacial defects, or controlled cathode doping profiles. They were chosen simply to give a representative set of Ohmic or nonOhmic cathode boundary conditions in order to reproduce various types

of space-charge behavior. Similar effects arise from mobility notches or barrier contacts.

Goto *et al.* [19] performed numerical computations on the domain dynamics in a planer Schottkey-gate Gunn device which was considered to be a fundamental structure as the Gunn-effect logic element because of good isolation between the input and output signals.

It can thus be said that the basic mechanism producing this effect is now well understood. Comprehensive reviews on the Gunn-effect device have been given by Carrol [39], Bulman, Hobson, and Taylor [40], Bosch and Engelmann [41], and Sze [42].

1.3 Gunn effect with impact ionization

The Gunn-effect device can yield chaotic current oscillations when it is driven by an external periodic force as shown in chapter 2. However, if the rf bias voltage is not imposed the Gunn-effect device may still exhibit non-periodic domain motion under some other additional conditions. For typical GaAs Gunn-effect devices, the energy required for impact ionization is considerably higher than that required for the intervalley electron transfer, which allows us to neglect the effect of impact ionization. On the other hand, in the case of the Gunn-effect device in narrow-gap semiconductors such as InSb, impact ionization is not negligible because of its low threshold field. For example, an irregular domain motion in an InSb Gunn diode was observed experimentally [43].

Čenys *et al.* studied this type of irregularity both analytically and numerically, suggesting that this irregularity is related to simultaneous existence of several domains resulting from competition between the Gunn instability and additional plasma wave instability due to impact ionization [44].

Ito *et al.* reported the formulation of multiple high-field domains and their chaotic behavior in InSb Gunn diode [45]. They showed that the multidomain regime emerges as a result of decrease in the domain size caused by impact ionization, and that destabilization of the multidomain regime leads to spatio-temporal chaos characterized by the Lyapunov dimension which increases with the system size.

Even in the GaAs Gunn-effect device, if it is highly doped and subject to a high bias voltage to such a degree that the electric field in the domain exceeds the threshold

value for the impact ionization, the carriers thus generated in an autocatalytic way will perturb the subsequent domain motion which in some cases gives rise to non-periodic current oscillations. Several experimental results suggest this really occurs in real systems in that the observed interpulse incoherence of the terminal current of the Gunn-effect device consisting of GaAs or InP is thought to be caused by the impact-ionization effect [16,32,33,46].

1.4 Recombination instability

Next, we consider oscillatory phenomena associated with the recombination instability which is caused by the field-enhanced trapping effect. This effect has been investigated by Gummel and Lax [47], Bonch-Bruevich [48], and Pratt and Ridley [49] to give its quantitative explanation. Ridley and Watkins [50,51] suggested that this effect could lead the system to NDC, and this type of NDC was observed in Sb-compensated Au-doped Ge by Ridley and Pratt [51-53].

For instance, in gold-doped n-Ge, the gold atoms are distributed as deep impurity levels in the form of doubly or triply charged negative ions. Trapped electrons are supplied by shallow donors which are considered to be empty at temperatures T~20-35K, *i.e.*, $2(N_t - N^-) + 3N^- = N_d$, where N_t, N^-, and N_d are the densities of total gold atoms, triply charged negative ions, and shallow donors respectively. Then the densities of doubly and triply charged negative ions are expressed by $(N_t - N^-) = 3N_t - N_d$ and $N^- = N_d - 2N_t$ respectively, and because these densities are always positive, therefore the condition $2N_t < N_d < 3N_t$ must be satisfied [4]. Under low excitation a large number of gold atoms exist as doubly charged negative ions, which can trap free electrons leading to the formation of triply charged negative ions. Since a free electron must penetrate the Coulomb potential barrier of the gold ion in order to be trapped by a doubly charged negative ion, the trapping(recombination) coefficient increases with the field E, which implies the field-enhanced trapping effect. By contrast, the emission of electrons is effectively field-independent as long as E is well below the threshold for the impact ionization. Thus the free electron density n decreases with increasing field: $\mathrm{d}n/\mathrm{d}E < 0$, and the differential

conductivity $\mathrm{d}J/\mathrm{d}E$ can become negative where $J(= -env)$ is the current density, e is the magnitude of electron charge, and v is the electron drift velocity. Thus a system has an N-shaped $J - E$ characteristics (NNDC), and this nonlinearity leads the system to a domain instability, namely, formation and propagation of the domain occur (the recombination instability) [4]. An experimental evidence that the recombination instability gives rise to slow current oscillations in gold or copper-doped n-Ge and high-resistivity GaAs was first reported by Stafeev [54] and Bonch-Bruevich and Kalashnikov [55].

The recombination instability and some properties of the electrical domains were investigated experimentally [56-60], and the results were in good qualitative agreement with the theory [61-64]. However, this type of domain instability seems to have attracted not so much attention as the case of the Gunn effect, since the oscillation frequency is very low ranging from a fraction of a hertz to several kilohertz (for sample length L=1cm) [4].

1.5 Chaos in semiconductors

The Gunn-effect oscillation is thus considered to be an example of dissipative structure in the sense that the system is operative in the state far from equilibrium driven by the electric field and that the nonlinearity of the current-voltage relation is indispensable for producing a spatio-temporal structure of the traveling domain. If such is the case, it will be quite natural to ask whether or not the Gunn-effect device gives rise to chaotic current oscillations under some suitably controlled conditions. Examples of the chaotic behavior have been reported in a great variety of disciplines [65]. Chaos in semiconductors can arise in different ways due to an intrinsic instability of the NDC element, and is one of the most recent examples of the chaotic behavior in physical systems. Although chaotic phenomena in semiconductors have in recent years attracted considerable attention, most of them appear to occur associated with the carrier generation accompanied by the impact ionization process especially for semiconductors with the current-controlled SNDC [1,66]. In contrast, to our knowledge, chaotic phenomena in Gunn-effect devices have not been studied experimentally with due attention, and the early simulational works on this subject were mainly devoted to obtaining information on the temporal evolution of the

Fourier mode variables [67].

Chaotic current oscillations can be caused by the carrier generation due to the impact ionization, as mentioned in section 1.3.

In the 1980s chaotic current oscillations caused by the recombination instability have been reported experimentally and theoretically [68-71]. However, in the theoretical treatment the system has been assumed to be spatially uniform and described by ordinary differential equations. Hence, the numerical simulations have been performed only to elucidate the temporal behavior of the system. As we have mentioned above, the current oscillation is closely connected with the domain motion, so it is very important to construct a model describing the corresponding system appropriately in terms of partial differential equations in which the spatial degrees of freedom are taken into account.

1.6 Composition of following chapters

In the following three sections, we give the results of our numerical simulations for the systems which exhibit current oscillations due to the domain instabilities under strong excitation conditions. We describe the system using the partial differential equations and pursue spatio-temporal behavior of the model system by the finite-difference method. In general, three types of modes of operation: the Ohmic, the quenched, and the transit-time modes are found. Non-periodic oscillations are also found in the transition region between the quenched and the transit-time modes. Their origins are clarified on the basis of spatio-temporal evolution of the high-field domain throughout this thesis.

In chapter 2, spatio-temporal evolution of the Gunn-effect device system subject to the dc and the rf alternating fields is computed with the amplitudes and the frequency being taken as the control parameters. Current oscillations associated with the cyclic traveling high-field domain are shown to materialize over a range of the control parameters. In particular, the current oscillations become chaotic at specially chosen values of these bias parameters.

In chapter 3, we discuss the behavior of the Gunn-effect device with the impact ionization. We thereby show the system exhibits non-periodic behavior due to its own au-

tonomous nonlinearity even if it is not driven by an external periodic field. The domain motion is perturbed by the carrier generation due to the impact ionization, and it becomes non-periodic for specially chosen parameters. It also exhibits interpulse incoherent current oscillations similar to those observed experimentally. Some remarks are given on the mechanism giving rise to the nonperiodicity on the basis of spatio-temporal evolution of the domain.

In chapter 4, we present a one-dimensional system of gold-doped n-Ge in which the recombination instability leads the system to instability and current oscillations. Spatio-temporal evolution of the high-field domain is computed with the bias voltage, the recombination coefficient, and the emission coefficient being taken as the control parameters.

Finally, a brief summary and conclusion are given in chapter 5.

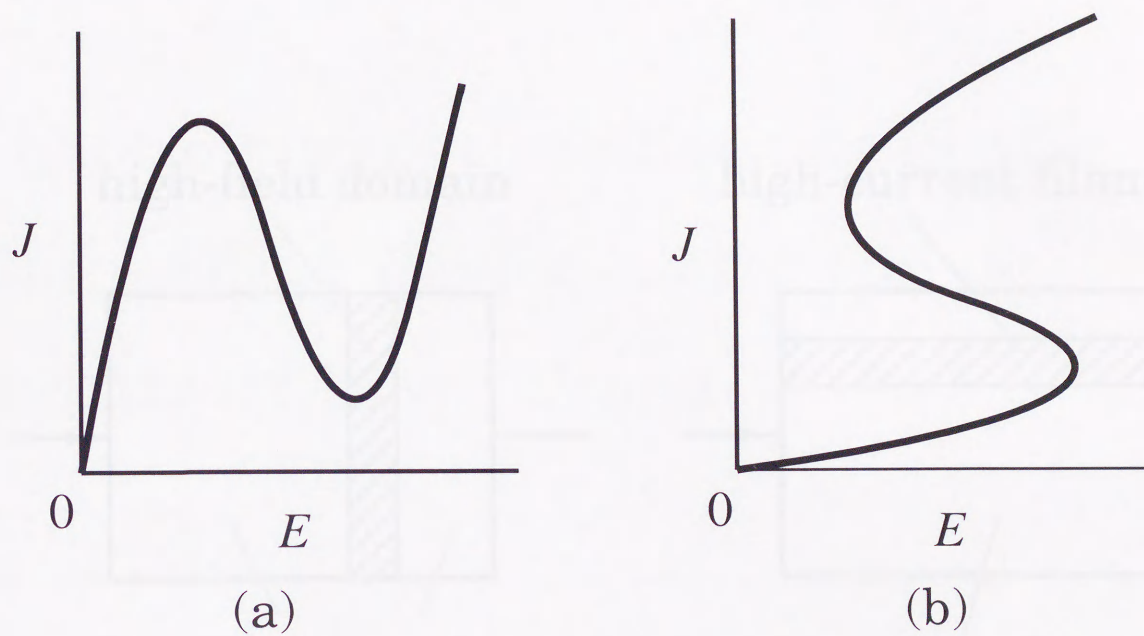

Figure 1.1 The two types of negative differential conductivity (NDC) in current density versus electric field characteristics: (a) N-shaped NDC (b) S-shaped NDC.

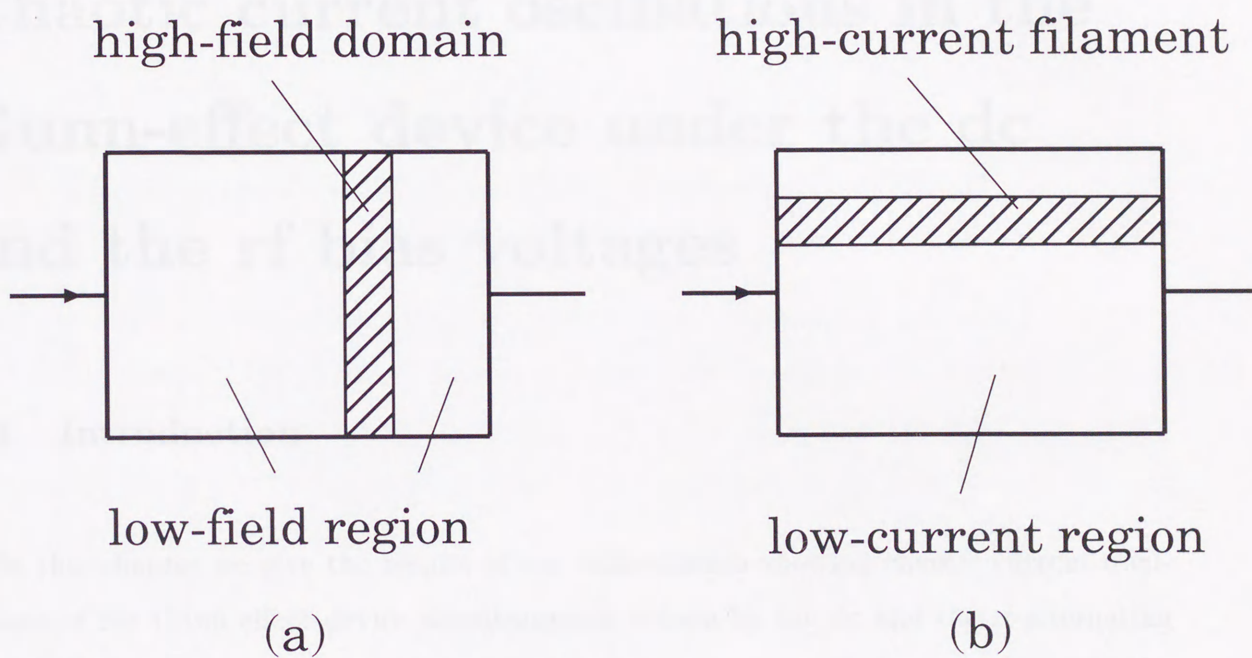

Figure 1.2 Formation of high-field domain in NNDC (a), and high-current filament in SNDC (b).

Chapter 2

Chaotic current oscillations in the Gunn-effect device under the dc and the rf bias voltages

2.1 Introduction

In this chapter we give the results of our computation showing chaotic current oscillations of the Gunn-effect device simultaneously driven by the dc and the rf-alternating fields [78]. Evolution of the one-dimensional model system for n-GaAs was pursued by the finite-difference method particularly to elucidate spatio-temporal behavior of the domain. In the bulk of our model system, electrons move in the form of high-field domain against uniformly doped donor background. There have been quite a few attempts to give an appropriate cathode boundary condition describing domain nucleation. The boundary condition is constructed on the basis of a doping notch where the donor-doping density is reduced in a certain manner near the cathode end of the device [12,18,28,72]. This gives a simple domain nucleating mechanism near the cathode without the inclusion of an external circuit containing resistance and battery. In the next section, formulation of the problem is given with a view to presenting the system of equations of motion, mathematical characterization of the device media, and numerical methods used to solve the equations. In section 2.3, we give the computational results for the dc-field driven Gunn-effect device

showing the three different regimes of operation: the Ohmic, the transit-time, and the quenched modes. The computations were performed to check that our scheme gives the results consistent with those obtained in other device simulations [15,49]. In section 2.4, we give the results of the computations performed for the system simultaneously driven by the dc and the rf-alternating fields and show the system undergoes period-doubling cascade to chaos over a range of the field parameters centered around a set of specially chosen values.

2.2 Equations of motion and the method of solution

We consider a one-dimensional system of the Gunn-effect device consisting of an n^+-n-n^+ GaAs sandwich structure. The system is assumed to occupy the region $0 < x < L$ with the cathode and the anode being at $x = 0$ and $x = L$ respectively. The electric current density $J(x,t)$ at the position x and time t is defined as the sum of the drift term and the diffusion term and is given by

$$J(x,t) = -en(x,t)v(E(x,t)) + eD\frac{\partial n(x,t)}{\partial x} \tag{2.1}$$

where $n(x,t)$ is the electron carrier density, $E(x,t)$ is the electric field, v is the electron drift velocity, e is the magnitude of electronic charge equal to 1.6×10^{-19}[C], and D is the diffusion coefficient. The electric potential $\Phi(x,t)$ is defined by

$$E(x,t) = -\frac{\partial \Phi(x,t)}{\partial x} \tag{2.2}$$

and the potential and the particle density are related by the Poisson equation

$$\frac{\partial^2 \Phi(x,t)}{\partial x^2} = -\frac{e}{\epsilon}(N_{\mathrm{d}}(x) - n(x,t)) \tag{2.3}$$

where ϵ is the dielectric constant and $N_{\mathrm{d}}(x)$ is the donor-doping density which is assumed to be time-independent. Time evolution of the carrier density is governed by the continuity equation

$$\frac{\partial n(x,t)}{\partial t} + \frac{\partial}{\partial x}\left(\frac{J(x,t)}{-e}\right) = 0. \tag{2.4}$$

For a velocity-field characteristic $v(E)$ of GaAs, use is made of a simple formula derived on the basis of a single electron temperature model [42]. Let μ_1 and μ_2 be the mobility at the lower and the upper valley respectively, ΔE the energy separation between the two valleys, R the ratio of the upper to the lower valley density of states, $T_{\rm L}$ the lattice temperature, $\tau_{\rm e}$ the dielectric relaxation time, and k the Boltzmann constant. The formula gives the relation $v(E)$ in terms of the electron temperature $T_{\rm e}$ in the form

$$v(E) = \frac{\mu_1 + \mu_2 R \exp(-\frac{\Delta E}{kT_{\rm e}})}{1 + R\exp(-\frac{\Delta E}{kT_{\rm e}})} \mid E \mid \tag{2.5}$$

$$E^2 = \frac{3k}{2e\tau_{\rm e}}(T_{\rm e} - T_{\rm L})\frac{1 + R\exp(-\frac{\Delta E}{kT_{\rm e}})}{\mu_1 + \mu_2 R\exp(-\frac{\Delta E}{kT_{\rm e}})} \tag{2.6}$$

where eq.(2.6) is numerically solved to yield $T_{\rm e}$ as a function of E and substitution of this $T_{\rm e}(E)$ into eq.(2.5) gives v as a function of E. The parameters for specifying GaAs under the room temperature operating conditions are taken as follows [42]: $\mu_1 = 6200[{\rm cm}^2/{\rm V{\cdot}s}]$, $\mu_2 = 50[{\rm cm}^2/{\rm V{\cdot}s}]$, $\Delta E = 0.31[{\rm eV}]$, $R = 94$, $T_{\rm L} = 300[{\rm K}]$, $\tau_{\rm e} = 1 \times 10^{-12}[{\rm s}]$. The result for the $v(E)$ curve thus obtained is shown in Fig. 2.1.

On the other hand, the donor-doping density $N_{\rm d}(x)$ used in this chapter is shown in Fig. 2.2. Taking into account the n^+-n-n^+ sandwich structure, we assume it to take the following form for the normalized total length $L = 60$

$$N_{\rm d}(x) = \begin{cases} 20N_0 & (0 < x < 2) \\ N_0[\frac{79}{3} - \frac{19}{6}x] & (2 < x < 8) \\ N_0[1 - H_0\sin(\frac{\pi}{4}x)] & (8 < x < 12) \\ N_0 & (12 < x < 52) \\ N_0[\frac{19}{6}x - \frac{982}{6}] & (52 < x < 58) \\ 20N_0 & (58 < x < 60) \end{cases} \tag{2.7}$$

where N_0 denotes the uniform background donor density in the bulk low n region$(12 < x < 52)$. The highly doped n^+-layers extend over the cathode-adjacent$(0 < x < 8)$ and the anode-adjacent$(52 < x < 60)$ regions. The concaved region$(8 < x < 12)$ near the cathode is the doping notch from which domain nucleation and propagation occur where its depth is denoted by $H_0(0 < H_0 < 1)$. As mentioned in section 2.1 this was used by several authors to represent domain nucleation mechanism inherent in the device adjacent to the cathode.

In this chapter we deal with eqs.(2.1)-(2.4) to determine spatio-temporal evolution of the field variables $n(x,t), J(x,t), E(x,t)$, and $\Phi(x,t)$ subject to appropriate initial and boundary conditions. We discretize the system in the framework of the finite difference method and first divide the one-dimensional system into ℓ partitions. The notations used to express eqs.(2.1)-(2.4) in the non-dimensional form are as follows: the length of the system L, the length of an equally divided partition $\Delta x = L/\ell$, the uniform bulk doping density N_0, the peak drift velocity V_{p} in the $v(E)$ curve and the corresponding peak electric field E_{p}. The formulas (2.5) and (2.6) for $v(E)$ give the result that the drift velocity takes the peak value $V_{\mathrm{p}} = 1.44 \times 10^7$[cm/s] at the field $E_{\mathrm{p}} = 3.5 \times 10^3$[V/cm]. Using these parameters, the transformations by which eqs.(2.1)-(2.4) are expressed in the non-dimensional form are such that $x \to (\Delta x)x$, $t \to (\Delta x/V_{\mathrm{p}})t$, $n(x,t) \to N_0 n(x,t)$, $N_{\mathrm{d}}(x) \to N_0 N_{\mathrm{d}}(x)$, $v(x,t) \to V_{\mathrm{p}} V(x,t)$, $E(x,t) \to E_{\mathrm{p}} E(x,t)$, $\Phi(x,t) \to E_{\mathrm{p}} L \Phi(x,t)$, $J(x,t) \to eN_0 V_{\mathrm{p}} J(x,t)$, $D \to (\Delta x) V_{\mathrm{p}} D$. The resulting non-dimensional equations are given by

$$J(x,t) = -n(x,t)V(x,t) + D\frac{\partial n(x,t)}{\partial x} \tag{2.8}$$

$$E(x,t) = -\ell\frac{\partial \Phi(x,t)}{\partial x} \tag{2.9}$$

$$\frac{\partial^2 \Phi(x,t)}{\partial x^2} = S[n(x,t) - N_{\mathrm{d}}(x)] \tag{2.10}$$

$$\frac{\partial n(x,t)}{\partial t} - \frac{\partial J(x,t)}{\partial x} = 0 \tag{2.11}$$

where $S = eN_0(\Delta x)^2/\epsilon E_{\mathrm{p}} L$.

On the spatially discretized system, the variables $n(x,t)$, $N_{\mathrm{d}}(x)$ and $\Phi(x,t)$ are defined at both ends of each partition: $i\Delta x (i = 0, 1, \ldots, \ell)$, while the variables $E(x,t)$, $V(x,t)$ and $J(x,t)$ are defined at the middle points of each partition: $(i-1/2)\Delta x (i = 1, 2, \ldots, \ell)$. The time step of the system evolution is denoted by Δt in unit of $\Delta x/V_{\mathrm{p}}$ so that the field variables are defined on the time points $k\Delta t (k = 0, 1, 2, \ldots)$. For convenience, two schemes of finite difference are employed to numerically integrate eqs.(2.8)-(2.11). In the first scheme referred to as A below, eqs.(2.8)-(2.11) are discretized with the aid of the difference procedure which is spatially centered and temporally explicit. The resulting forms satisfied by the discretized variables whose position and time are designated by the subscript i and the superscript k respectively are found to be

$$J^k_{i+\frac{1}{2}} = -\frac{n^k_{i+1} + n^k_i}{2} V^k_{i+\frac{1}{2}} + D\frac{n^k_{i+1} - n^k_i}{\Delta x} \tag{2.12}$$

$$E^k_{i+\frac{1}{2}} = -\ell\frac{\Phi^k_{i+1} - \Phi^k_i}{\Delta x} \tag{2.13}$$

$$\Phi^k_{i+1} - 2\Phi^k_i + \Phi^k_{i-1} = (\Delta x)^2 S(n^k_i - (N_d)_i) \tag{2.14}$$

$$n^{k+1}_i = n^k_i + \frac{\Delta t}{\Delta x}(J^k_{i+\frac{1}{2}} - J^k_{i-\frac{1}{2}}). \tag{2.15}$$

If the time step Δt is taken sufficiently small, this scheme is expected to give a fairy good overall behavior of the system evolution. However, in a sensitive situation in which it is necessary to determine whether the relevant motion is periodic or nonperiodic, the scheme is often found to give a different type of motion depending on the different choice of Δt. In particular, it has been pointed out mathematically that the explicit finite difference scheme in some cases gives an unreliable approximation to the original differential equations thus leading to a difficulty in distinguishing chaos from regular motion [73]. In order to avoid such a possibility in a subtle case, we use a more refined scheme referred to as B. Substitution of eq.(2.8) in (2.11) gives

$$\frac{\partial n(x,t)}{\partial t} + \frac{\partial (n(x,t)V(x,t))}{\partial x} - D\frac{\partial^2 n(x,t)}{\partial x^2} = 0. \tag{2.16}$$

The governing equations thus become eqs.(2.9), (2.10), and (2.16). Discretization of eqs.(2.9) and (2.10) is performed in the same manner as in Scheme A leading to eqs.(2.13) and (2.14) respectively. As for eq.(2.16), the drift term is discretized using the second-order Lax-Wendroff method, while the diffusion term is transformed to the difference form using the Crank-Nicholson method. The results are expressed in the form of a successive two-step time progression via an intermediate grid at $(i + \frac{1}{2}, k + \frac{1}{2})$:

$$n^{k+\frac{1}{2}}_{i+\frac{1}{2}} = \frac{n^k_i + n^k_{i+1}}{2} - \frac{\Delta t}{2\Delta x}(n^k_{i+1}\frac{V^k_{i+1} + V^k_i}{2} - n^k_i\frac{V^k_i + V^k_{i-1}}{2}) \tag{2.17}$$

$$\begin{aligned} n^{k+1}_i = n^k_i - \frac{\Delta t}{\Delta x}(n^{k+\frac{1}{2}}_{i+\frac{1}{2}}V^k_i - n^{k+\frac{1}{2}}_{i-\frac{1}{2}}V^k_{i-1}) + \frac{D\Delta t}{2(\Delta x)^2}(n^{k+1}_{i+1} - 2n^{k+1}_i + n^{k+1}_{i-1}) \\ + \frac{D\Delta t}{2(\Delta x)^2}(n^k_{i+1} - 2n^k_i + n^k_{i-1}) \end{aligned} \tag{2.18}$$

where the Crank-Nicholson method introduces the semi-implicit time integration in eq.(2.18). The Scheme B thus consists of successive iterations using eqs.(2.13), (2.14), (2.17), and (2.18).

The equations of motion are integrated under the initial conditions

$$n(x,0) = N_\mathrm{d}(x) \quad \text{and} \quad \Phi(x,0) = \frac{x}{\ell}\Phi_\mathrm{dc} \tag{2.19}$$

and the boundary conditions

$$n(0,t) = N_\mathrm{d}(0) \quad , \quad n(\ell,t) = N_\mathrm{d}(\ell),$$
$$\Phi(0,t) = 0, \quad \text{and} \quad \Phi(L,t) = \Phi_\mathrm{dc} - \Phi_\mathrm{rf}\cos 2\pi f_0 t \tag{2.20}$$

where Φ_dc is the applied dc voltage across the device, Φ_rf is the maximum instantaneous rf voltage amplitude across the device, and f_0 is the frequency of the rf oscillation. The values of the system parameters which are kept to be fixed during the present computations are taken as $L = 6.0 \times 10^{-3}$[cm], $N_0 = 1.4 \times 10^{15}$[cm^{-3}], $V_\mathrm{p} = 1.44 \times 10^7$[cm/s], $E_\mathrm{p} = 3.5 \times 10^3$[V/cm], $D = 200$[cm^2/s], and $\epsilon = 12.4\epsilon_0 = 1.11 \times 10^{-12}$[F/cm]. These are considered to be typical of the usual GaAs Gunn-effect devices [42,49]. As for the parameters characterizing discretization, the number of the space partition ℓ_n is below assumed to be $\ell_\mathrm{n} = 300$ so that $\Delta x = L/300 = 2 \times 10^{-5}$[cm] and $\Delta x/V_\mathrm{p} = 1.39 \times 10^{-12}$[s]($\sim \tau_\mathrm{e}$). Under these conditions, the computations were performed to elucidate what kind of spatio-temporal behavior the system exhibits depending on the chosen values of the control parameters comprising Φ_dc, Φ_rf, and f_0.

2.3 The motion under the dc bias voltage

In this section we deal with the system operating under the dc bias voltage condition such that $\Phi(\ell,t) = \Phi_\mathrm{dc}$, and integrate the system using the Scheme A with $\Delta t = 0.05$. Referring to the results of former device simulations [18,28], we have taken the depth of the notch as $H_0 = 0.4$. Owing to extensive experimental and simulational investigations in the 1960s and the 1970s, it is now confirmed that the system exhibits several different modes of the motion depending on the imposed values of Φ_dc. We performed the computation for several values of Φ_dc in order to check the workability of the present model system by comparing the results with those available in the literature [39,40,43,49].

At lower values of Φ_dc the system exhibits steady-state behavior and the field variables turn out time-independent. This may be called the Ohmic or the steady mode, and the results at $\Phi_\mathrm{dc} = 10$[V] representing this operation are shown in Figs. 2.3(a) and 2.4(a). Under the perturbation of a uniform field δE, the steady electron density n which deviates

from the unperturbed value $n_0(= N_d)$ is determined by the equation $v\partial n_0/\partial x = -\delta n/\tau$, where $\delta n = n - n_0$, v is the drift velocity and τ is the associated relaxation time. This deviation δn is in turn related with the perturbed field δE via the Poisson equation $\partial\delta E/\partial x =\mid e \mid \delta n/\epsilon$. Since $v > 0$ in the present geometry, the two equations give the result that $\partial\delta E/\partial x > 0$(resp. < 0) and $\delta n > 0$(resp. < 0) over the region where $\partial n_0/\partial x < 0$(resp. > 0). This reasoning leads us to understand why the bump of the electric field (we call this "the remaining domain" below) appears as shown in Fig. 2.3(a) around the doping notch when the uniform dc field is imposed on the system.

At higher values of Φ_{dc} the system exhibits periodic current oscillations associated with a high-field domain cyclically propagating from the cathode to the anode. This is usually called the transit-time dipole mode. The computational results at $\Phi_{dc} = 30$[V] for this mode are shown in Figs. 2.3(c) and 2.4(c). In this case the dc-driven domain cycling frequency f_{dc} is found to be 2.4[GHz]. Nucleation of the domain occurs over the range of the doping notch where the bump of the electric field grows with increase of the applied field. If the electric field is sufficiently high so that the electron drift is characterized by a negative differential mobility, a perturbed electric field imposed on this region causes the growth of an electron accumulation layer preceded by its depletion layer, *i.e.*, a high-field dipole domain. Furthermore, under a sufficiently high bias the domain thus nucleated detaches itself from the cathode and moves downward towards the anode (we call this "the traveling domain" below).

At intermediate values of Φ_{dc} only part of the domain is detached from the cathode and a growth competition between the traveling and the remaining domains occurs. If the bias voltage is insufficient, the traveling domain drains within the bulk of the device before reaching the anode. This releases the part of the bias voltage distributed thus far to the traveling domain and again causes the growth of the remaining domain at the notch. The growth continues until it again breaks up, thereby involving partial domain detachment. The cycle thus repeats itself and is called the quenched dipole mode. The results representing this mode of the motion at $\Phi_{dc} = 12$[V] are shown in Figs. 2.3(b) and 2.4(b).

We have thus found the present computations give the results that the system exhibits three different modes of operation denoted by the Ohmic, the quenched and the transit-

time mode as the dc bias $\Phi_{\rm dc}$ is increased, which is in agreement with the results of the previous computations due to Grubin *et al.* for the uniformly doped system connected with the external circuit containing resistance and the emf battery [15,49]. Incidentally, the time evolution of the current density at the anode $J(\ell, t)$ for these three modes is shown in Fig. 2.5. In addition, for reference below, the result in Fig. 2.6 shows how appearance of the different modes of motion depends on the dc voltage $\Phi_{\rm dc}$ and the depth of the doping notch H_0.

2.4 The motion under the dc and rf bias voltage

In this section we deal with the system driven by the bias voltage $\Phi(\ell, t) = \Phi_{\rm dc} - \Phi_{\rm rf}\cos 2\pi f_0 t$. The chart given by Fig. 2.6 suggests that some peculiar mode of motion is expected to occur when the values of $\Phi(\ell, t)$ are driven in such a way that the system alternates between the period of the transit-time and the quenched modes. For convenience, the relevant parameters H_0 and $\Phi_{\rm dc}$ are assumed to be such that $H_0 = 0.4$ and $\Phi_{\rm dc} = 30$[V] so that the motion in the absence of the rf bias is dominated by the transit-time mode with $f_{\rm dc} = 2.4$[GHz] as shown in section 2.3. With the aid of numerical simulations we tried to find out the peculiar motion of the type mentioned above over a range of the control parameters $\Phi_{\rm rf}$ and f_0. For this purpose, the parameters $\Phi_{\rm dc}$ and $\Phi_{\rm rf}$ are chosen to satisfy the conditions under which the motion is dominated by the transit-time and the quenched modes when $\Phi(\ell, t)$ takes the dc value $\Phi_{\rm dc}$ and the minimum value $\Phi_{\rm dc} - \Phi_{\rm rf}$ respectively. As a result of rather extensive computational work on the basis of parameter search over a range of $\Phi_{\rm rf}$ and f_0 centered around quite a few different sets of their starting values, we here give the results for two cases where (i) the system exhibits a quasi-periodic motion with the subharmonic frequency and that (ii) the system undergoes period-doubling cascade leading to chaos. It is found in both cases that the cyclic motion driven by the dc voltage is entrained by the externally driven oscillations and that the resultant synchronous motion is characterized by the rf frequency f_0. The results are presented with the aid of the power sperctral densities(PSD) and bird's-eye views of spatio-temporal evolution of the field profile. All the PSDs in this chapter are expressed

in the arbitrary units, and plotted on a logarithmic scale.

2.4.1 Quasi-periodic behavior

This is the case in which f_0 is set equal to 1.2[GHz] and $\Phi_{\rm rf}$ is varied over a range of the values around 11[V]. The computations were carried out using Scheme B with the time interval $\Delta t = 0.05$. The PSDs in Figs. 2.7 show that the motions at $\Phi_{\rm rf} = 11$[V] and 11.5[V] are quasi-periodic accompanied with the fractional subharmonic frequency $f_0/7$ and $f_0/12$ respectively. Spatio-temporal evolution of the domain given by Figures 2.8(a) and (b) show that the motion is dominated by a mixture of the transit-time and the quenched modes and that the profiles develop a complicated fine structure over the long period $7/f_0$ and $12/f_0$ respectively. This may be accounted for by the fact that, since $f_0 < f_{\rm dc}$ in this case, extinction of the domain within the bulk occurs for part of the longer period $1/f_0$.

2.4.2 Period-doubling cascade

This is the case in which f_0 is set equal to 8.0[GHz] and $\Phi_{\rm rf}$ is varied over a range of the values below 17[V]. The computations were carried out using Scheme B with the time interval $\Delta t = 0.01$. The reason for the choice of this rather fine size of Δt is that we are here in a delicate situation in which we must determine whether the system develops chaos or not. The reliability of the scheme we here use is somewhat guaranteed by the fact that the computations performed for some typical cases using $\Delta t = 0.005$ and 0.01 were found to give the results with almost the same order of accuracies.

Figures 2.9(a)-(i) show a series of the PSD for the current density at the anode $J(\ell, t)$ obtained with the decrease of $\Phi_{\rm rf}$ below 17[V]. Figure 2.9(a) indicates that the system at $\Phi_{\rm rf} = 17$[V] exhibits the periodic motion characterized by the driving frequency f_0. Spatio-temporal evolution of the domain shown in Fig. 2.10(a) reveals that the periodic oscillation of the terminal current is a manifestation of the prevailing quenched mode. This appears to occur because propagation of the traveling domain cannot be sustained for part of the original period $1/f_{\rm dc}$ due to the condition $f_0 > f_{\rm dc}$. With a decrease of $\Phi_{\rm rf}$ to 14[V] the system undergoes a period doubling bifurcation as is clearly shown in Fig. 2.9(b). This is associated with the salient spatio-temporal behavior shown in Fig. 2.10(b)

where two domains travel with a certain distance apart and drain almost simultaneously at the different points within the bulk away from the anode. Further decrease of $\Phi_{\rm rf}$ entails the forward and the subsequent reverse period-doubling cascades between which the motion at $\Phi_{\rm rf} = 12.2[\mathrm{V}]$ is found to be chaotic. Ultimately, only a slight decrease of $\Phi_{\rm rf}$ from $10[\mathrm{V}]$ to $9.999[\mathrm{V}]$ gives rise to a transition from the motion with the subharmonic frequency $f_0/2$ to that with $f_0/3$.

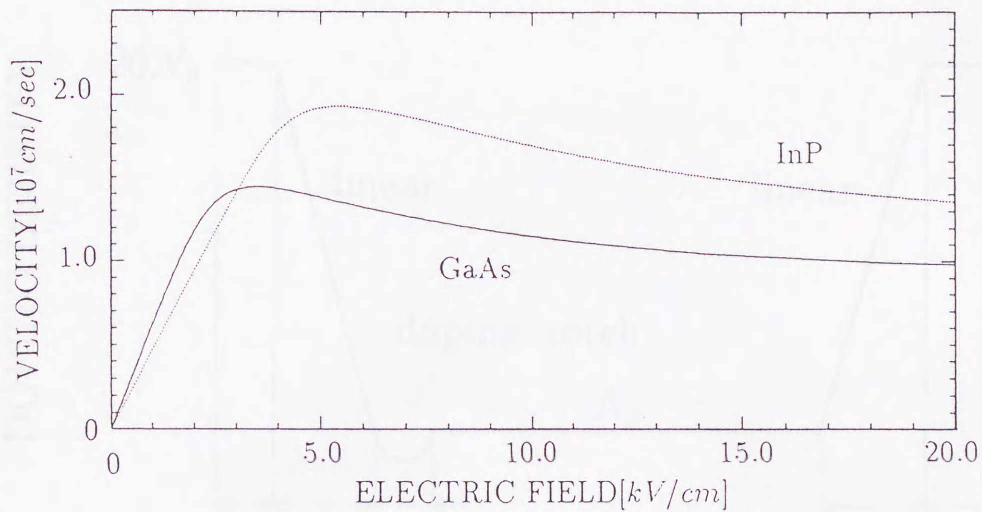

Figure 2.1 Velocity-field characteristic $v(E)$ for GaAs calculated by the formula (2.5)-(2.6) at 300K. Also shown for reference is that for InP. The material data used here are those given in Ref [42].

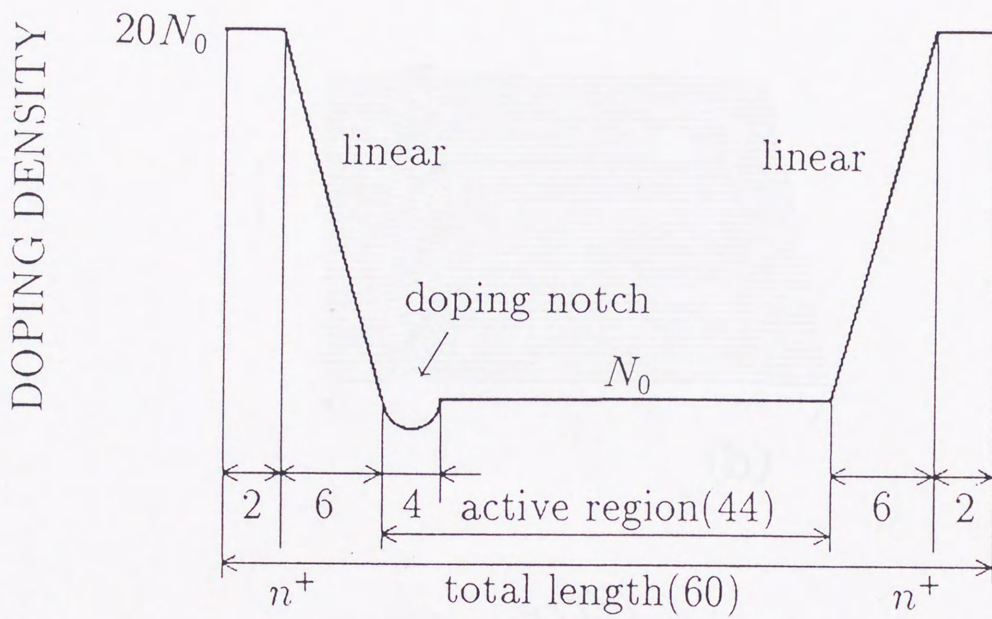

Figure 2.2 Device doping profile used in the computation where the total length is normalized to be 60.

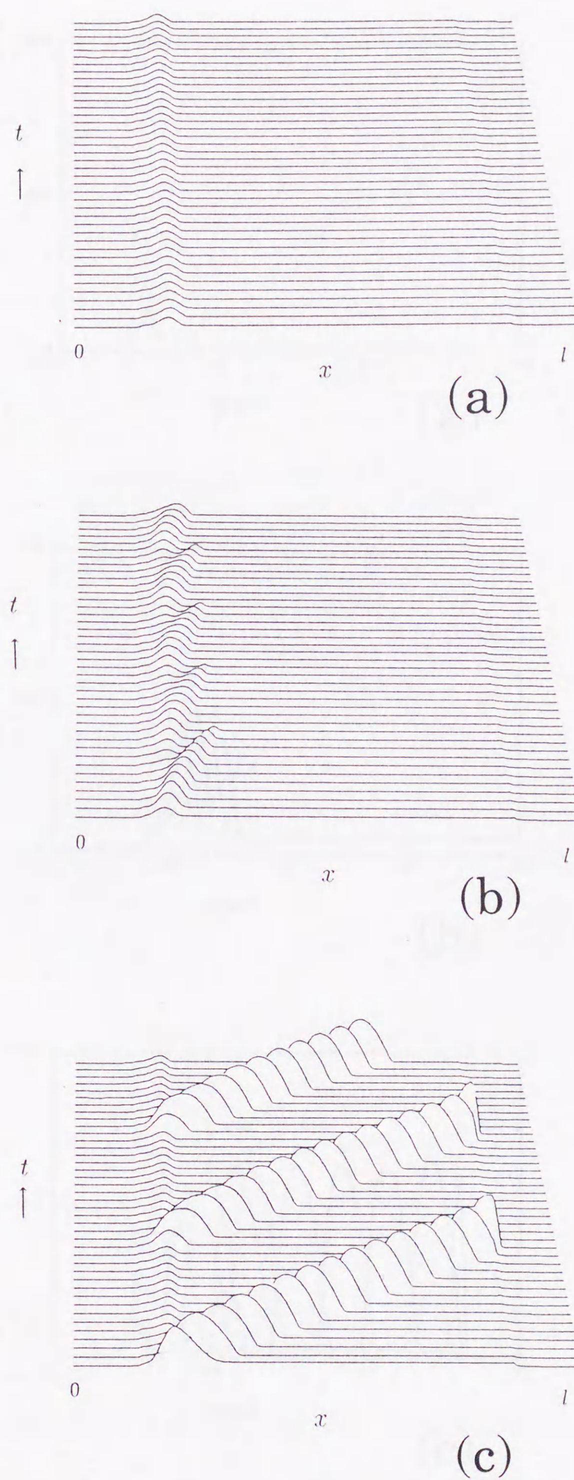

Figure 2.3 Spatio-temporal evolution of the electric field $E(x, t)$ for the dc-driven case $\Phi(l, t) = \Phi_{\mathrm{dc}}$. (a) $\Phi_{\mathrm{dc}} = 10$[V], (b) 12[V], (c) 30[V]. Time between successive vertical display is such that (a) $400\Delta t$, (b) $100\Delta t$, and (c) $400\Delta t$, where the time step Δt is taken as 0.05 in unit of $\Delta x/V_{\mathrm{p}}$.

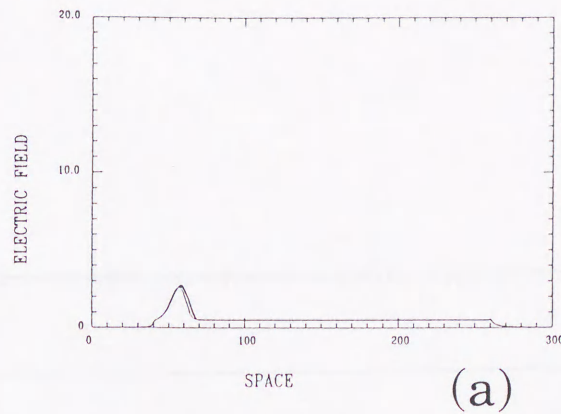

(a)

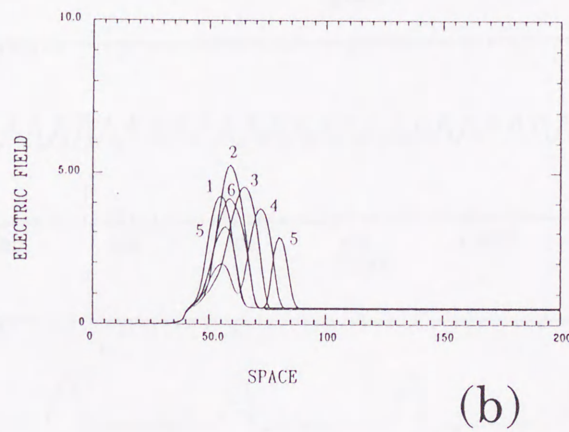

(b)

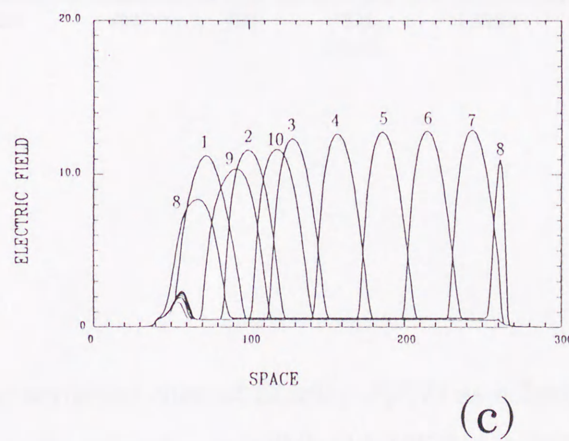

(c)

Figure 2.4 Time evolution of the field profiles $E(x,t)$ which proceeds according to the order of the number attached to each profile. (a) $\Phi_{\rm dc} = 10$[V], (b) 12[V], (c) 30[V]. Time between successive profiles is such that (b) $200\Delta t$ and (c) $800\Delta t$.

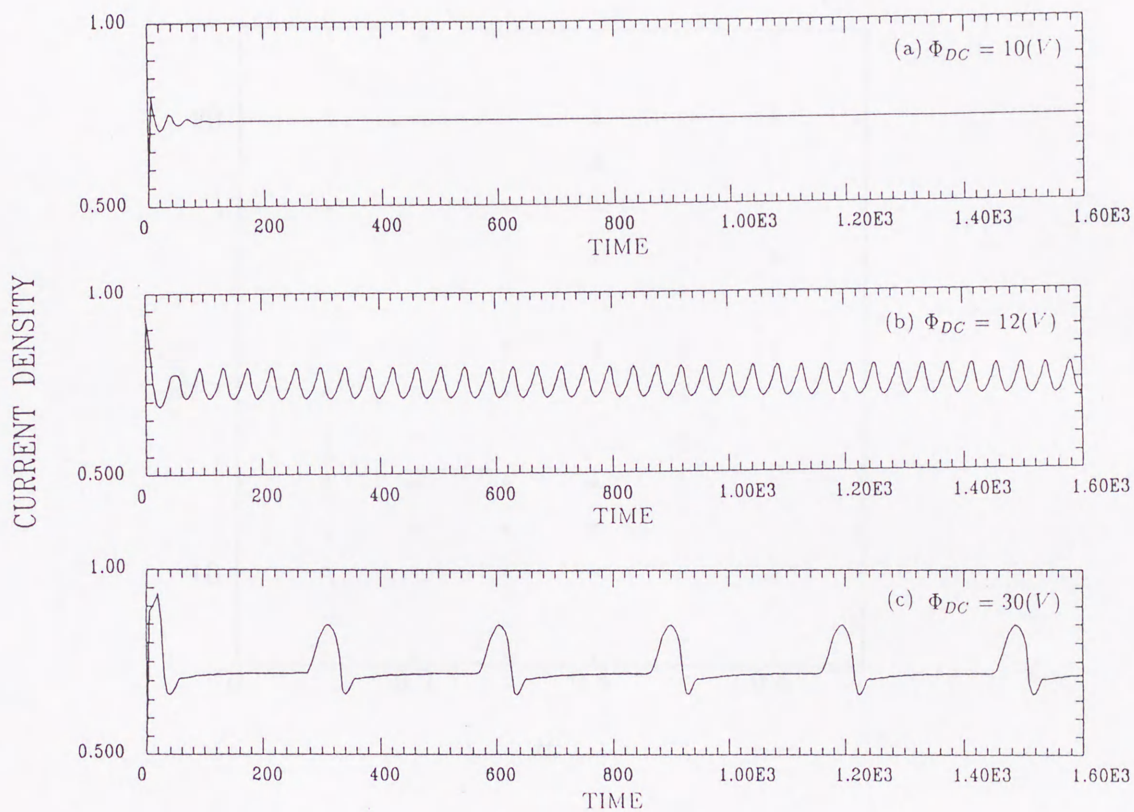

Figure 2.5 The terminal current density $J(\ell, t)$ as a function of the time t for the dc-driven case $\Phi(\ell, t) = \Phi_{\mathrm{dc}}$: (a) $\Phi_{\mathrm{dc}} = 10$[V], (b) 12[V], (c) 30[V].

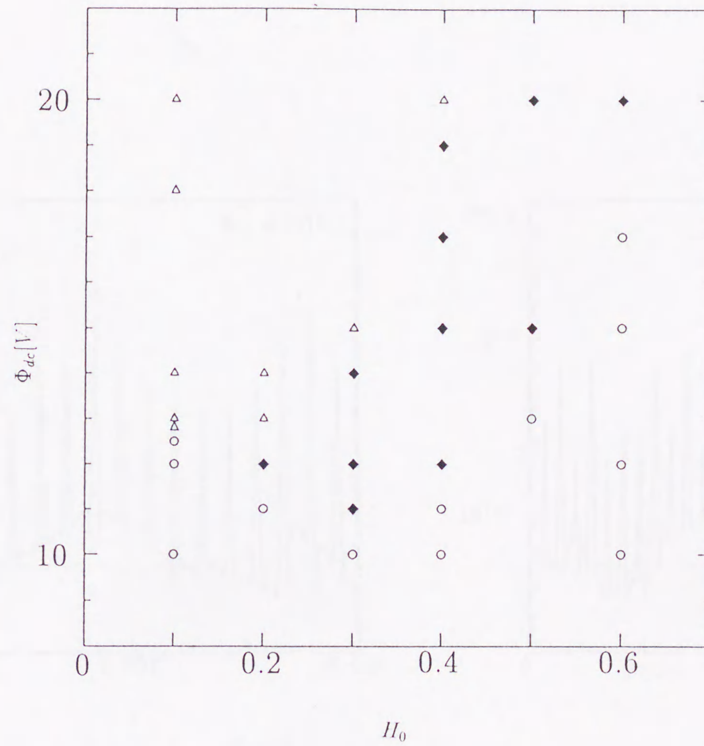

Figure 2.6 The dc bias voltage Φ_{dc}[V] and the depth of the doping notch H_0 are plotted to show the values appropriate to the Ohmic(open circles), the quenched(solid diamonds), and the transit-time(open triangles) modes.

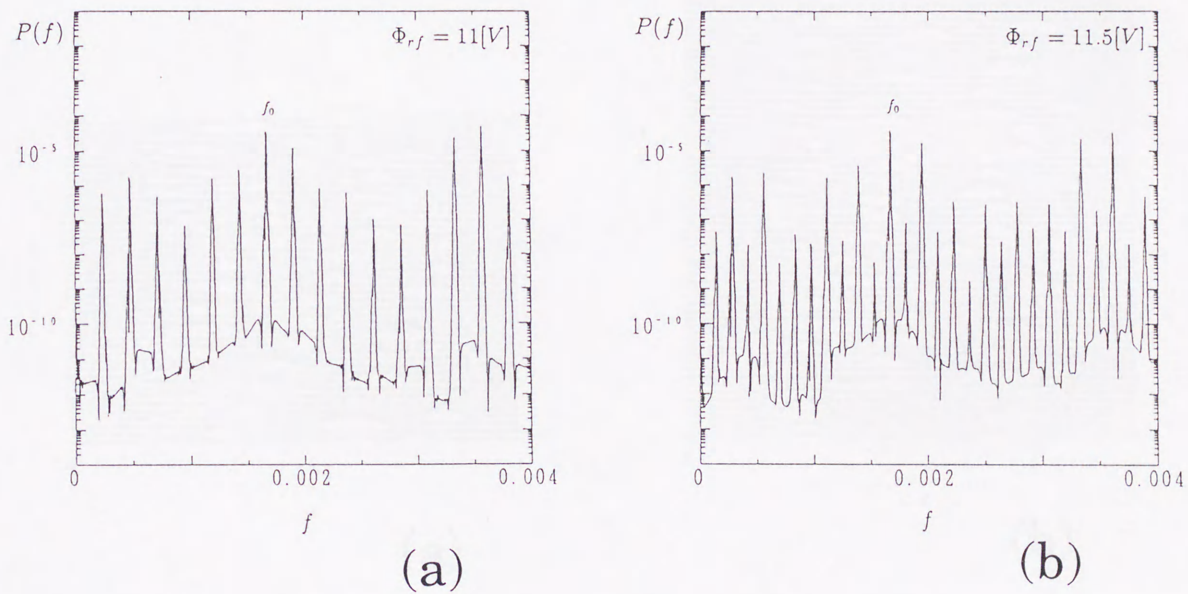

Figure 2.7 The PSD $P(f)$ as a function of f for the terminal current $J(\ell, t)$ for the dc- and rf-driven case with $\Phi_{\mathrm{dc}} = 30$[V] and $f_0 = 1.2$[GHz]. The rf amplitude is varied in unit of V such that (a) $\Phi_{\mathrm{rf}} = 11$, (b) 11.5. The abscissa measures the frequency in unit of $V_{\mathrm{p}}/\Delta x$.

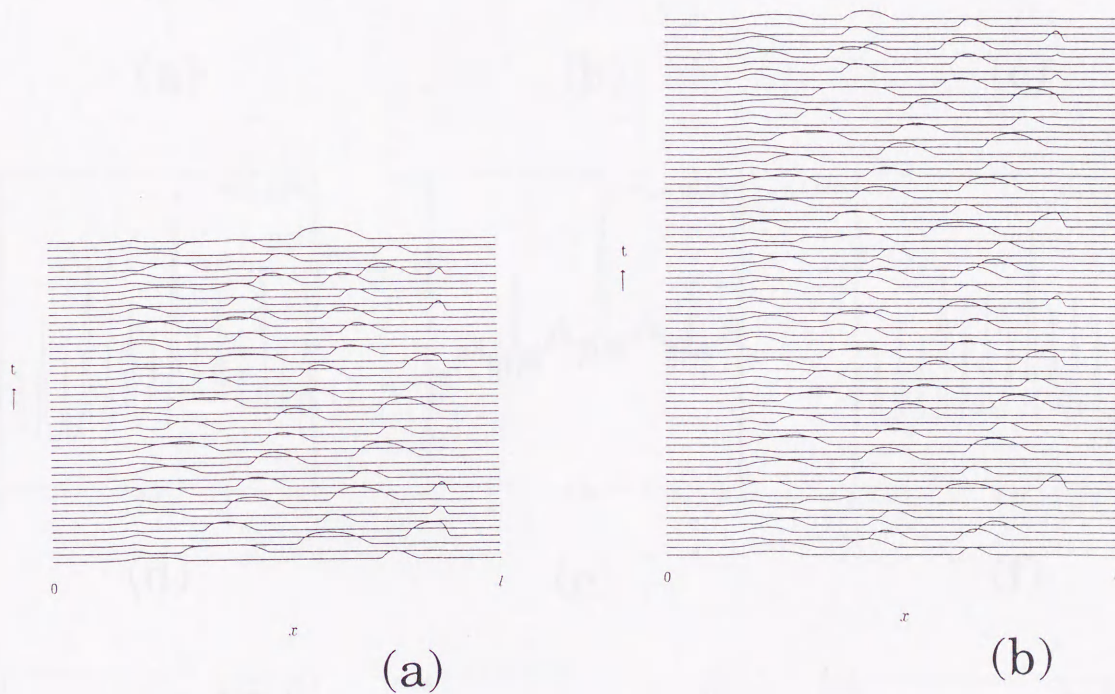

Figure 2.8 Spatio-temporal evolution of the electric field $E(x,t)$ for the dc- and rf-driven case with $\Phi_{dc} = 30$[V] and $f_0 = 1.2$[GHz]. (a) $\Phi_{rf} = 11$[V], (b) 11.5[V]. Time between successive vertical display is $2000\Delta t$ with $\Delta t = 0.05$ in unit of $\Delta x/V_p$. Shaded lines are not eliminated for better tracing the profile evolution. Time between the bottom and the top horizontal lines is the inverse of the subharmonic frequency, *i.e.*, the period of the slower mode.

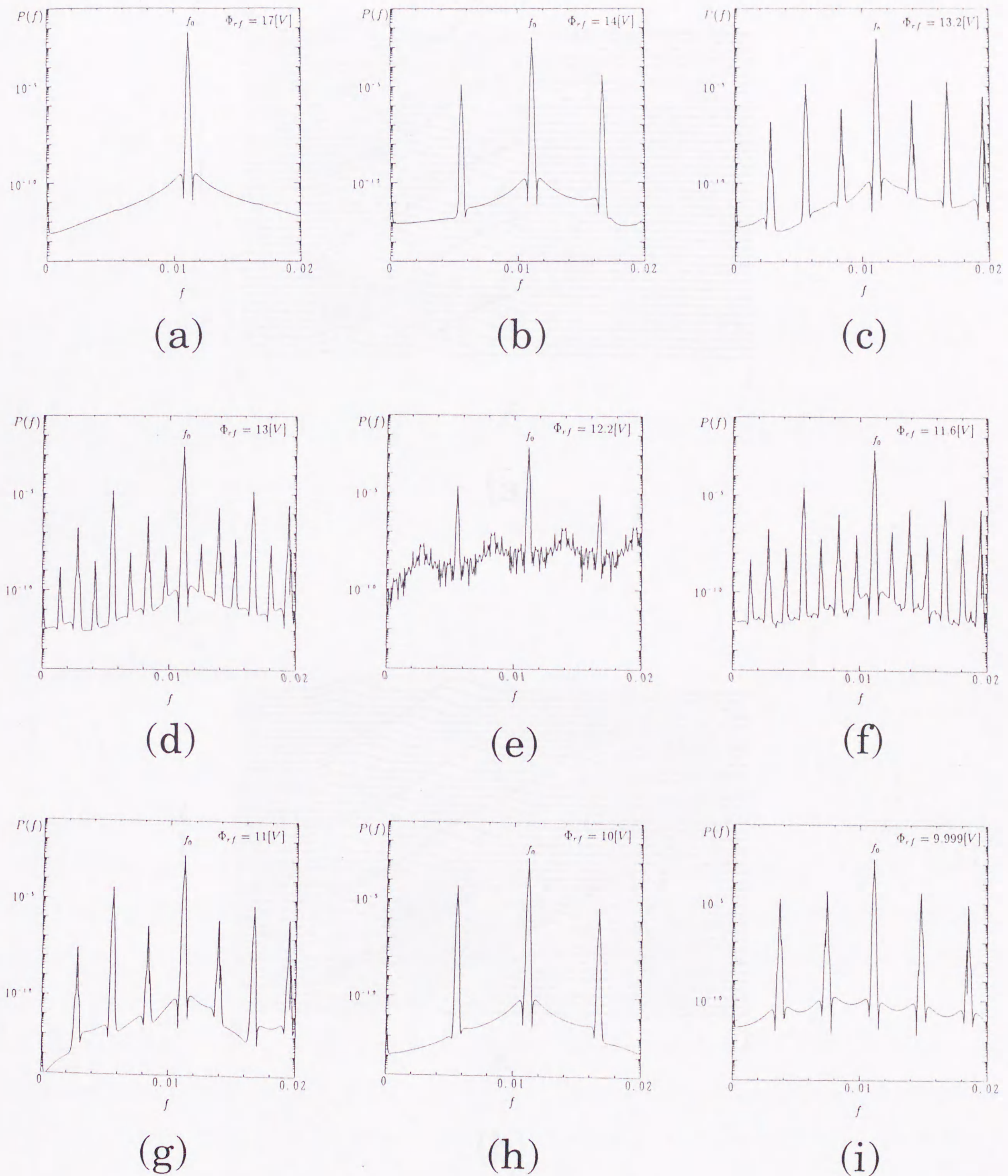

Figure 2.9 The PSD $P(f)$ as a function of f for the terminal current $J(\ell, t)$ for the dc- and rf-driven case with $\Phi_{\rm dc} = 30$[V] and $f_0 = 8.0$[GHz]. The rf amplitude is varied in unit of V such that (a) $\Phi_{\rm rf} = 17$, (b) 14, (c) 13.2, (d) 13.0, (e) 12.2, (f) 11.6 (g) 11.0, (h) 10.0, (i) 9.999. The abscissa measures the frequency in unit of $V_{\rm p}/\Delta x$.

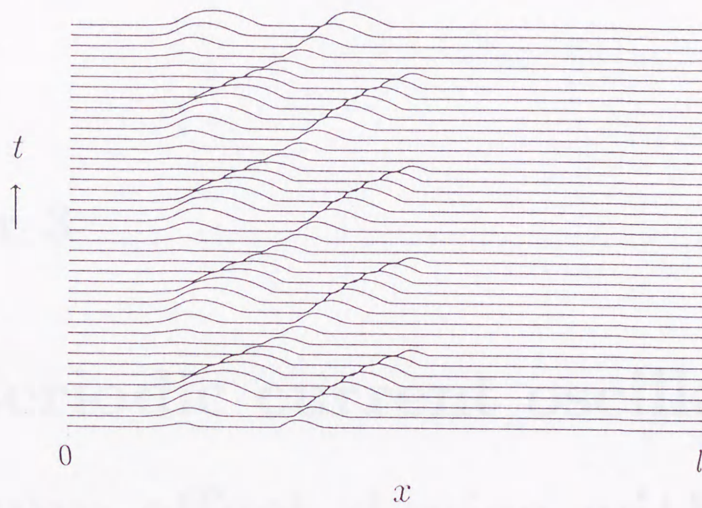

(a)

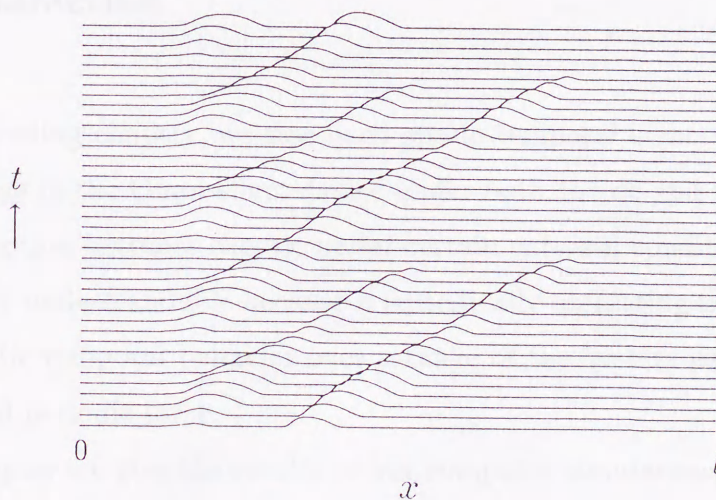

(b)

Figure 2.10 Spatio-temporal evolution of the electric field $E(x,t)$ for the dc- and rf-driven case with $\Phi_{\rm dc} = 30$[V] and $f_0 = 8$[GHz]. (a) $\Phi_{\rm rf} = 14$[V], (b) 17[V]. Time between successive vertical display is $1000\Delta t$ with $\Delta t = 0.01$ in unit of $\Delta x/V_{\rm p}$.

Chapter 3

Non-periodic current oscillations in the Gunn-effect device with the impact-ionization effect

3.1 Introduction

In the preceding chapter, we discussed spatio-temporal structure of the traveling domain appearing in the Gunn-effect device under both the dc and the rf bias voltages and showed the motion becomes chaotic under certain external conditions [74,75,85]. The results are easily understandable because a periodically oscillating nonlinear system usually exhibits chaotic temporal behavior over a range of the system parameters if it is driven by an external periodic force.

In this chapter we give the results of our computer simulations for the case where the system is assumed to consist of GaAs [84] whose threshold value for the impact ionization is much higher than that of InSb. Since the domain motion is regular in the absence of the impact ionization for the case of GaAs, we can examine the effect of the impact ionization by which the motion becomes irregular by gradually increasing or decreasing the associated model parameters. In section 3.2 formulation of the problem is given with a view to presenting a system of equations of motion, mathematical characterization of the device media and numerical methods used to solve the equations. In section 3.3 we

give the results of our computations for the system with the impact-ionization effect and show the system exhibits complicated spatio-temporal behavior.

3.2 Equations of motion and the method of solution

In addition to the system which we treated in the preceding chapter, we here take into account the effect of the impact ionization and the dynamics for holes which are created by the impact ionization.

The total *electric* current density $J(x,t)$ at the position x and the time t is expressed using the *particle* current densities for electrons $Q_{\mathrm{N}}(x,t)$ and holes $Q_{\mathrm{P}}(x,t)$ in the form

$$J(x,t) = -eQ_{\mathrm{N}}(x,t) + eQ_{\mathrm{P}}(x,t). \tag{3.1}$$

Each particle current density is defined as the sum of the drift term and the diffusion term

$$Q_{\mathrm{N}}(x,t) = n(x,t)v_{\mathrm{N}}(E(x,t)) - D_{\mathrm{N}}\frac{\partial n(x,t)}{\partial x} \tag{3.2}$$

$$Q_{\mathrm{P}}(x,t) = -p(x,t)v_{\mathrm{P}}(E(x,t)) - D_{\mathrm{P}}\frac{\partial p(x,t)}{\partial x} \tag{3.3}$$

where $p(x,t)$ is the hole carrier density, v_{N} and v_{P} are the electron and the hole drift velocities respectively, D_{N} and D_{P} are the diffusion constants for electrons and holes respectively.

The electric potential $\Phi(x,t)$ is thus defined by

$$E(x,t) = -\frac{\partial \Phi(x,t)}{\partial x} \tag{3.4}$$

and the potential and the particle densities are related by the Poisson equation

$$\frac{\partial^2 \Phi(x,t)}{\partial x^2} = -\frac{e}{\epsilon}(N_{\mathrm{d}}(x) + p(x,t) - n(x,t)). \tag{3.5}$$

Time evolution of the carrier densities is governed by the continuity equations

$$\frac{\partial n(x,t)}{\partial t} + \frac{\partial Q_{\mathrm{N}}(x,t)}{\partial x} = G_0 - \gamma_0\{n(x,t)p(x,t) - N_{\mathrm{int}}^2\} \tag{3.6}$$

$$\frac{\partial p(x,t)}{\partial t} + \frac{\partial Q_{\mathrm{P}}(x,t)}{\partial x} = G_0 - \gamma_0\{n(x,t)p(x,t) - N_{\mathrm{int}}^2\} \tag{3.7}$$

with

$$G_0 = g_0 \exp\left[-\left(\frac{E_{\rm th}}{E(x,t)}\right)^2\right]\{|Q_{\rm N}|+|Q_{\rm P}|\} \tag{3.8}$$

where γ_0 is the recombination rate, g_0 is the impact-ionization rate, and $E_{\rm th}$ is the threshold field for the impact ionization. $N_{\rm int}(\equiv \sqrt{n_{\rm eq}p_{\rm eq}})$ is the intrinsic density where $n_{\rm eq}$ and $p_{\rm eq}$ are equilibrium electron and hole densities respectively, and this term represents thermal carrier generation independent of the electric field, that is, the reverse process against that for the pair annihilation [80]. In eqs.(3.6),(3.7) the first and the second terms of the rhs express the carrier generation due to the impact ionization and the carrier annihilation due to the recombination respectively. A more detailed account of these terms are given in section 3.3.

The forms of the velocity-field characteristics $v_{\rm N}(E)$ and $v_{\rm P}(E)$ we use in this chapter are taken as follows. For $0< E <20$ [kV/cm], $v_{\rm N}(E)$ is given by the same formula derived in section 2.2. In the present case where the impact ionization takes place, the local electric field becomes much higher than 20 [kV/cm]. Unfortunately, for the electric field larger than about 20 [kV/cm], $v(E)$ characteristics is not well established either theoretically or experimentally. As the electric field is so high that the impact ionization occurs, the drift velocity is considered to be independent of the field, *i.e.* it corresponds to the saturated velocity v_{SN}. For the electric fields between 20 and 40 [kV/cm] the electron drift velocity is assumed to decrease linearly down to the saturated velocity $v_{\rm NS} = 0.8\times10^7$[cm/s]. For the electric fields above 40[kV/cm] the velocity is assumed to be independent of the field and equal to $v_{\rm NS}$ [76]. On the other hand, the hole velocity $v_{\rm P}(E)$ is assumed to be linear ($\mu_{\rm low} = 400$ [cm^2/V·s]) for the electric fields between 0 and 20 [kV/cm], and to be equal to $v_{\rm NS}$ above 20[kV/cm] [76].

The donor-doping density $N_{\rm d}(x)$ is assumed to take the same profile as in chapter 2.

In this chapter we deal with eqs.(3.1)-(3.8) to determine spatio-temporal evolution of the field variables $n(x,t), p(x,t), Q_{\rm N}(x,t), Q_{\rm P}(x,t), E(x,t)$, and $\Phi(x,t)$ subject to appropriate initial and boundary conditions.

We discretize the system in the same framework of the finite difference method as in the preceding chapter and first divide the one-dimensional system into l partitions. The notations used to express eqs.(3.1)-(3.8) in the non-dimensional form are as follows: the length of the system L, the length of an equally divided partition $\Delta x = L/l$, the uniform

bulk doping density N_0, the maximum drift velocity V_M in the $v_N(E)$ and $v_P(E)$ curve and the corresponding electric field E_M. Using these parameters, the transformations by which eqs.(3.1)-(3.8) are expressed in the non-dimensional form are such that $x \to (\Delta x)x$, $t \to (\Delta x/V_M)t$, $n(x,t) \to N_0 n(x,t)$, $p(x,t) \to N_0 p(x,t)$, $N_d(x) \to N_0 N_d(x)$, $v_N(x,t) \to V_M V_N(x,t)$, $v_P(x,t) \to V_M V_P(x,t)$, $E(x,t) \to E_M E(x,t)$, $\Phi(x,t) \to E_M L \Phi(x,t)$, $J(x,t) \to eN_0 V_M J(x,t)$, $Q_N(x,t) \to N_0 V_M Q_N(x,t)$, $Q_P(x,t) \to N_0 V_M Q_P(x,t)$, $N_{int} \to N_0 N_{int}$, $D_N \to (\Delta x) V_M D_N$, $D_P \to (\Delta x) V_M D_P$. The resulting non-dimensional equations are given by

$$J(x,t) = -Q_N(x,t) + Q_P(x,t) \tag{3.9}$$

$$Q_N(x,t) = n(x,t)V_N(x,t) - D_N \frac{\partial n(x,t)}{\partial x} \tag{3.10}$$

$$Q_P(x,t) = -p(x,t)V_P(x,t) - D_P \frac{\partial p(x,t)}{\partial x} \tag{3.11}$$

$$E(x,t) = -l \frac{\partial \Phi(x,t)}{\partial x} \tag{3.12}$$

$$\frac{\partial^2 \Phi(x,t)}{\partial x^2} = S(n(x,t) - p(x,t) - N_d(x)) \tag{3.13}$$

$$\frac{\partial n(x,t)}{\partial t} + \frac{\partial Q_N(x,t)}{\partial x} = G - \gamma \left\{ n(x,t)p(x,t) - N_{int}^2 \right\} \tag{3.14}$$

$$\frac{\partial p(x,t)}{\partial t} + \frac{\partial Q_P(x,t)}{\partial x} = G - \gamma \left\{ n(x,t)p(x,t) - N_{int}^2 \right\} \tag{3.15}$$

$$G = g \exp\left[-\left(\frac{E_{th}}{E(x,t)} \right)^2 \right] \{ |Q_N| + |Q_P| \} \tag{3.16}$$

where the non-dimensional parameters are defined by $S = eN_0(\Delta x)^2/\epsilon E_M L$, $g = (\Delta x) g_0$, and $\gamma = N_0(\Delta x)\gamma_0/V_M$.

Substitution of eqs.(3.10) and (3.11) into (3.14) and (3.15) respectively gives

$$\frac{\partial n(x,t)}{\partial t} + \frac{\partial n(x,t)V_N(x,t)}{\partial x} - D_N \frac{\partial^2 n(x,t)}{\partial x^2} = G - \gamma \left\{ n(x,t)p(x,t) - N_{int}^2 \right\} \tag{3.17}$$

$$\frac{\partial p(x,t)}{\partial t} - \frac{\partial p(x,t)V_P(x,t)}{\partial x} - D_P \frac{\partial^2 p(x,t)}{\partial x^2} = G - \gamma \left\{ n(x,t)p(x,t) - N_{int}^2 \right\}. \tag{3.18}$$

The governing equations thus become eqs.(3.12),(3.13), and (3.18)-(3.20). On the spatially discretized system, the variables $n(x,t)$, $p(x,t)$, $N_d(x)$, and $\Phi(x,t)$ are defined at both ends of each partition: $i\Delta x (i = 0, 1, \cdots, l)$, while the variables $E(x,t)$, $V_N(x,t)$, $V_P(x,t)$, $Q_N(x,t)$, and $J_P(x,t)$ are defined at the middle points of each partition: $(i - 1/2)\Delta x (i = 1, 2, \cdots, l)$. The time step of the system evolution is denoted by Δt in unit of

$\Delta x/V_{\mathrm{M}}$. Equations. (3.10)-(3.18) are discretized with the same procedure as the preceding chapter, and result in the following form:

$$(Q_{\mathrm{N}})_i^k = \frac{n_i^k + n_{i-1}^k}{2}(V_{\mathrm{N}})_i^k - D_{\mathrm{N}}\frac{n_i^k - n_{i-1}^k}{\Delta x} \tag{3.19}$$

$$(Q_{\mathrm{P}})_i^k = -\frac{p_i^k + p_{i-1}^k}{2}(V_{\mathrm{P}})_i^k - D_{\mathrm{P}}\frac{p_i^k - p_{i-1}^k}{\Delta x} \tag{3.20}$$

$$E_{i+(1/2)}^k = -l\frac{\Phi_{i+1}^k - \Phi_i^k}{\Delta x} \tag{3.21}$$

$$\Phi_{i+1}^k - 2\Phi_i^k + \Phi_{i-1}^k = (\Delta x)^2 S(n_i^k - p_i^k - (N_{\mathrm{d}})_i). \tag{3.22}$$

$$n_{i+(1/2)}^{k+(1/2)} = \frac{n_i^k + n_{i+1}^k}{2} - \frac{\Delta t}{2\Delta x}\left(n_{i+1}^k\frac{(V_{\mathrm{N}})_{i+1}^k + (V_{\mathrm{N}})_i^k}{2} - n_i^k\frac{(V_{\mathrm{N}})_i^k + (V_{\mathrm{N}})_{i-1}^k}{2}\right) \tag{3.23}$$

$$p_{i+(1/2)}^{k+(1/2)} = \frac{p_i^k + p_{i+1}^k}{2} + \frac{\Delta t}{2\Delta x}\left(p_{i+1}^k\frac{(V_{\mathrm{P}})_{i+1}^k + (V_{\mathrm{P}})_i^k}{2} - p_i^k\frac{(V_{\mathrm{P}})_i^k + (V_{\mathrm{P}})_{i-1}^k}{2}\right) \tag{3.24}$$

$$\begin{aligned} n_i^{k+1} &= n_i^k - \frac{\Delta t}{\Delta x}(n_{i+(1/2)}^{k+(1/2)}(V_{\mathrm{N}})_i^k - n_{i-(1/2)}^{k+(1/2)}(V_{\mathrm{N}})_{i-1}^k) + \frac{D\Delta t}{2(\Delta x)^2}(n_{i+1}^{k+1} - 2n_i^{k+1} + n_{i-1}^{k+1}) \\ &+ \frac{D\Delta t}{2(\Delta x)^2}(n_{i+1}^k - 2n_i^k + n_{i-1}^k) + \frac{G_i^k + G_{i-1}^k}{2} - \gamma\left\{n_i^k p_i^k - (N_{\mathrm{int}})^2\right\} \end{aligned} \tag{3.25}$$

$$\begin{aligned} p_i^{k+1} &= p_i^k + \frac{\Delta t}{\Delta x}(p_{i+(1/2)}^{k+(1/2)}(V_{\mathrm{P}})_i^k - p_{i-(1/2)}^{k+(1/2)}(V_{\mathrm{P}})_{i-1}^k) + \frac{D\Delta t}{2(\Delta x)^2}(p_{i+1}^{k+1} - 2p_i^{k+1} + p_{i-1}^{k+1}) \\ &+ \frac{D\Delta t}{2(\Delta x)^2}(p_{i+1}^k - 2p_i^k + p_{i-1}^k) + \frac{G_i^k + G_{i-1}^k}{2} - \gamma\left\{n_i^k p_i^k - (N_{\mathrm{int}})^2\right\} \end{aligned} \tag{3.26}$$

$$G_i^k = g\exp\left[-\left(\frac{E_{\mathrm{th}}}{E_i^k}\right)^2\right]\left\{|(Q_{\mathrm{N}})_i^k| + |(Q_{\mathrm{P}})_i^k|\right\} \tag{3.27}$$

where the Crank-Nicholson method introduces the semi-implicit time integration in eqs.(3.25) and (3.26). The scheme thus consists of successive iterations using eqs.(3.19)-(3.27).

The equations of motion are integrated under the initial conditions

$$n(x,0) = N_{\mathrm{d}}(x),\ p(x,0) = 0,\ \text{and}\ \Phi(x,0) = \frac{x}{l}\Phi_{\mathrm{dc}} \tag{3.28}$$

and the boundary conditions

$$n(0,t) = N_{\mathrm{d}}(0), \quad n(l,t) = N_{\mathrm{d}}(l), \quad p(0,t) = p(l,t) = 0$$

and

$$\Phi(0,t) = 0, \quad \Phi(l,t) = \Phi_{\mathrm{dc}}. \tag{3.29}$$

The values of the system parameters which are kept to be fixed during the present computations are taken as $L = 6.0\times10^{-3}$[cm], $N_0 = 5.0\times10^{15}$[cm^{-3}], $V_{\mathrm{M}} = 1.69\times10^7$[cm/s],

$E_M = 3.01 \times 10^3$[V/cm], $D_N = 2.0 \times 10^2$[cm^2/s], $D_P = 2.0 \times 10$[cm^2/s], and $\epsilon = 13.1\epsilon_0 = 1.17 \times 10^{-12}$[F/cm] where V_M and E_M are determined by the formulas (2.5) and (2.6). The parameters characterizing time discretization is $\Delta x/V_M = 1.18 \times 10^{-12}$[s]($\sim \tau_e$). Under these conditions, the computations were performed for several chosen values of the control parameters Φ_{dc} and γ_0.

If we deal with the system operating without the impact-ionization effect, namely, in case the system is described by a single-carrier model (only electrons) and the governing equations are given by eqs. (3.10) and (3.12)-(3.14), we recover the results of section 2.3.

3.3 Simulational results

We here give the results of our numerical simulations carried out to find peculiar modes of motion which are expected to occur when the electric field in the domain exceeds the threshold value for the impact ionization. This involves autocatalytic carrier generation which in some cases leads to complicated system evolution. Experimental determination of the ionization rate has been made by several research groups [76,81]. There is a general, though not universal, agreement that the ionization rates of electrons and holes (denoted as α_N and α_P respectively) for GaAs are equal. As shown in eq.(3.8) we in this work use an expression for the ionization rates of the form [76,81]

$$\alpha_N = \alpha_P = \alpha(E) = g_0 \exp\left[-\left(\frac{E_{th}}{E}\right)^2\right] \qquad (3.30)$$

which expresses an abrupt increase in the carrier density with increase of the electric field E in excess of the threshold value E_{th}. In this chapter the coefficients are taken as $g_0 = 1.0 \times 10^5$[cm^{-1}] and $E_{th} = 1.0 \times 10^5$[V/cm]. Although these are slightly different from the values given by Hall and Leck ($g_0 = 2.0 \times 10^5$[cm^{-1}] and $E_{th} = 5.5 \times 10^5$[V/cm]) [81], our coefficients are assumed to have qualitatively similar effects on the simulational results. The carrier generation rate G is assumed to be proportional to the sum of the absolute values of the particle current densities for electrons and holes. As for the recombination rate, we use the form given by the second term of the rhs of eqs.(3.14) and (3.15). The value of the recombination coefficient γ_0 used in this chapter is taken to be larger than that

expected by the direct band-to-band radiative recombination rate ($\sim 10^{-10}$[cm^3/s]) [82]. Although the rate of recombination is experimentally determined to be $\gamma \sim 10^{-10}$[cm^3/s] for highly doped systems whose carrier concentration is 10^{17}[cm^{-3}] or more [83], the value of γ_0 for the system with concentration of 10^{15} [cm^{-3}] which is the value used in the present model, is not available to our knowledge. We have found from our computational results that for $\gamma_0 \sim 10^{-10}$[cm^3/s] the recombination is too weak to compensate the carrier-generation due to the impact ionization and that the carrier density increases indefinitely to such a degree that formation and propagation of the stable high-field domain is no longer sustainable. This may represent one of the cases observed by Heeks [33]. We below restrict ourselves to the cases where the recombination rate is taken to be sufficiently strong so that well-defined domain propagation is noticeable. In this sense we take γ_0 simply as the model parameter under the assumption that other faster recombination processes arising from the impurity levels, the defects and so on may possibly occur in real systems.

Among the results of extensive computational work carried out with the parameters varied over a wide range of Φ_{dc} and γ_0, we here give the ones for the two cases where (i) the bias voltage is taken to be low in such a way that the system without the impact ionization exhibits the quenched mode and that (ii) the bias voltage is taken to be sufficiently high so that the system exhibits the transit-time mode. In both cases the motion becomes very complicated and the associated current oscillations are found to be non-periodic.

3.3.1 Case for low Φ_{dc}

This is the case in which Φ_{dc} is set equal to 12[V]. As shown in Figs. 3.2(a) and (b) the motion in the absence of the impact ionization occurs in the form of the quenched mode. The parameter γ_0 is chosen as 1.0×10^{-5}[cm^3/s] and 1.0×10^{-6}[cm^3/s].

Figures 3.4(a)-(d) show the results for $\gamma_0 = 1.0 \times 10^{-5}$[cm^3/s]. From the current density time series Fig. 3.4(a), we find that the motion is nearly periodic, though the time intervals between the neighboring peaks or the bottoms of the current waveform and the associated amplitudes are slightly different from one another. This seems to occur as a slight modulation of the carrier density generation arising from the impact ionization in the domain near the cathode. This is considered to be the case where the rate of pair

creation is almost in equilibrium with that of recombination so that the motion of the domain is hardly perturbed by the impact-ionization effect.

Figures 3.5(a)-(d) show the results for a slower recombination rate $\gamma_0 = 1.0\times10^{-6}[\mathrm{cm}^3/\mathrm{s}]$. The traveling domain moves a long way further to the anode as compared with the preceding case. This seems to arise from the following reasons. The holes which are generated due to the impact ionization in the domain move in the direction (opposite to electrons) toward the cathode and accumulate near the cathode. This can be seen from Fig. 3.5(c) in that the hole density remains finite between the notch and the traveling domain. Since the rate of recombination is weaker than the preceding case, the number of these holes only slowly diminishes. The surviving holes suppress the growth of the remaining domain occurring at the notch near the cathode to such a degree that the remaining domain at the notch cannot quench the traveling domain. Thus the traveling domain moves a long way from the cathode.

The current density time series Fig. 3.5(a) resembles that of the transit-time mode given by Fig. 3.3(a). However, the intervals between the neighboring pulses in Fig. 3.5(a) are different from each other, by which we suspect the system exhibits an interpulse incoherence similar to those observed experimentally [16,32,33,49]. The pulse of current oscillations is usually generated when the domain is quenched. Figure 3.5(b) shows the quenched points are different from each other. This seems to be the reason for the interpulse incoherence.

3.3.2 Case for high Φ_{dc}

This is the case in which Φ_{dc} is set equal to 20[V]. As shown in Figs. 3.3(a) and (b) the motion occurs in the form of a transit-time mode, if the impact ionization is not included. The parameter γ_0 is chosen as $1.0\times10^{-5}[\mathrm{cm}^3/\mathrm{s}]$ and $1.0\times10^{-6}[\mathrm{cm}^3/\mathrm{s}]$.

Figures 3.6(a)-(d) show the results for $\gamma_0 = 1.0 \times 10^{-5}[\mathrm{cm}^3/\mathrm{s}]$. Figure 3.6(a) shows that the intervals between the neighboring pulses become narrow and unequal as compared with Fig. 3.3(a), and resembles those of Fig. 3.5(a) in that it also seemingly represents the interpulse incoherent current density. In this case, however, the impact ionization occurs quite frequently in the domain because of the high bias voltage. The domain consists of the electron accumulation layer preceded by the depletion layer. Most of the

generated electrons fill part of the depletion layer and most of the generated holes are annihilated in recombination with the electrons in the accumulation layer where its rate γ_0 is faster than that of the case given by Figs. 3.5. Accompanied by this process the growth of the remaining domain at the notch region is curtailed and the domain detaches the notch region with its height only insufficiently grown as compared with that for the case without the impact ionization. In fact, the traveling domain size in Fig. 3.6(b) is smaller than that in Fig. 3.2(b). Furthermore, the remaining domain persists on a scale not negligibly small and the growth competition between the traveling and the remaining domains occurs under the conditions seemingly not so unfavorable to the remaining one, so the traveling domain is quenched midway before reaching the anode. It is to be noted that the sum of the areas shared by the traveling and the remaining domains represents the bias voltage kept constant in our system.

Figures 3.7(a)-(d) show the case for $\gamma_0 = 1.0 \times 10^{-6}[\mathrm{cm}^3/\mathrm{s}]$. Of the four cases given in this section, this is the case where the bias voltage is highest but the rate of recombination is slowest. The motion is very complicated and the current density oscillates very violently. The domains are nucleated anywhere in the device not restricted to the region near the notch and quenched similarly anywhere. We cannot notice any relation between the pulse peaks of the current oscillations and the quenched point of the traveling domain. For this case we have not yet found any reasonable explanation for the complicated interactions between the traveling and the remaining domains under the strong influence of the carrier generation due to the impact ionization.

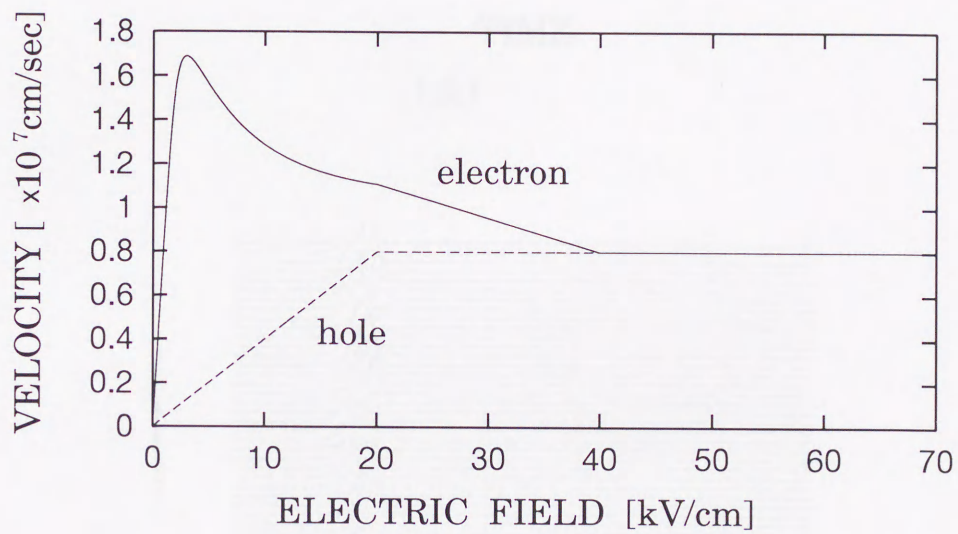

Figure 3.1 Velocity-field characteristics of GaAs for the electron $v_N(E)$ and the hole $v_P(E)$ where $v_N(E)$ is calculated by the formula (3.9)-(3.10). The material data used here are those given in ref.[42] and [76].

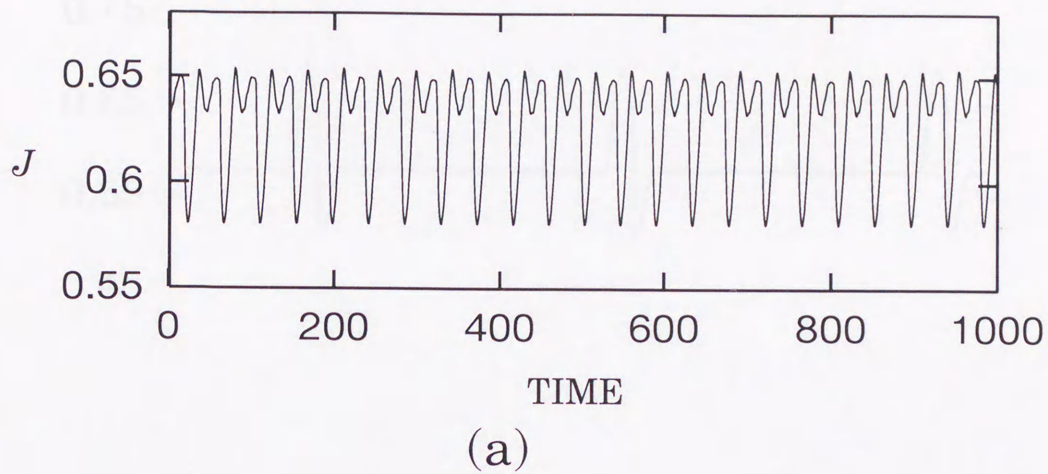

(a)

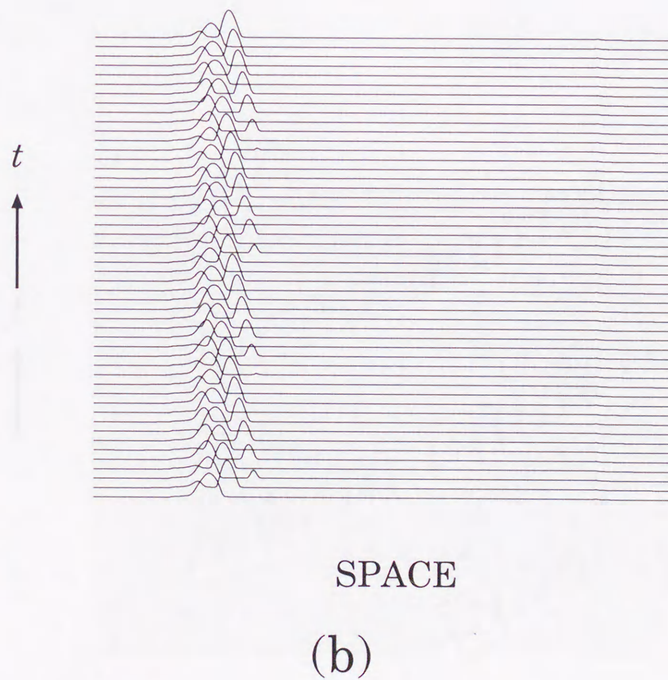

(b)

Figure 3.2 The quenched mode solution for the case Φ_{dc}=12[V] without the impact-ionization effect. (a)The non-dimensional total current density at the anode $J(l,t)$ as a function of time t. The ordinate is measured in arbitrary unit. (b)Spatio-temporal evolution of the electric field $E(x,t)$. Time between successive vertical display is $2000\Delta t$ where Δt is taken as 0.01 in unit of $\Delta x/V_P$.

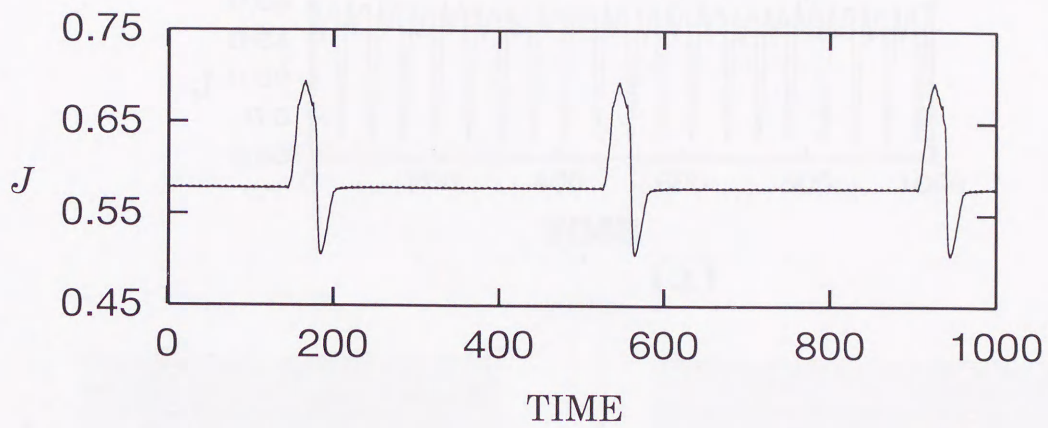

(a)

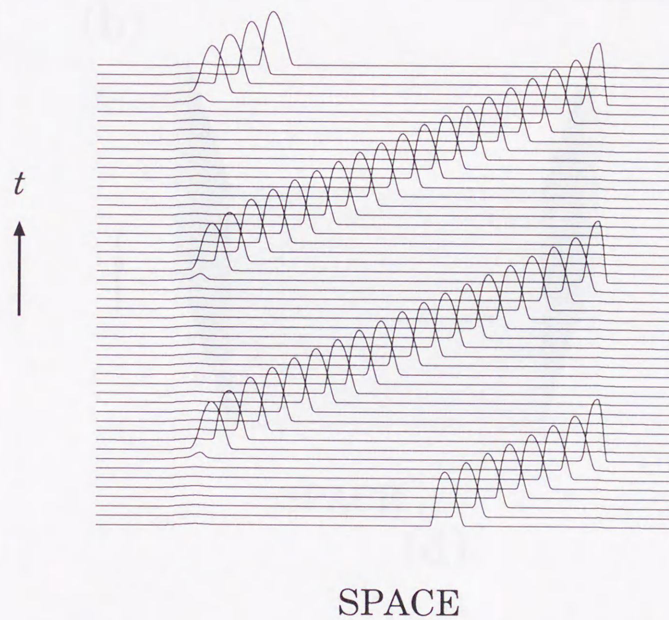

(b)

Figure 3.3 The same as Fig. 3.2 for the transit-time mode solution for the case Φ_{dc}=20[V] without the impact-ionization effect.

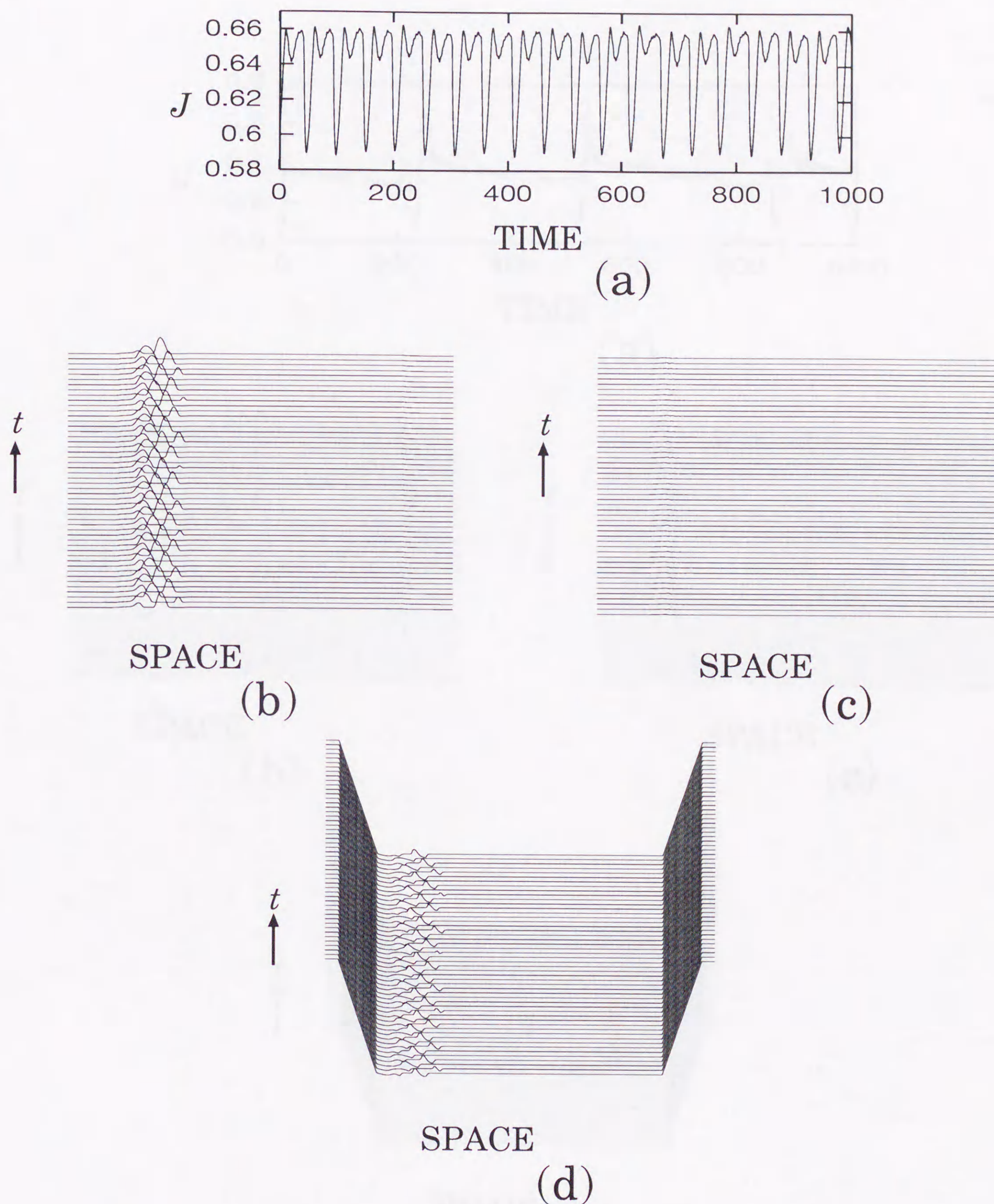

Figure 3.4 The motion for the case Φ_{dc}=12[V] and $\gamma_0 = 1.0 \times 10^{-5}$[cm^3/s] with the impact-ionization effect. (a)The non-dimensional total current density at the anode $J(l,t)$ as a function of time t. The ordinate is measured in arbitrary unit. (b),(c),(d)Spatio-temporal evolution of the electric field $E(x,t)$, the hole density $P(x,t)$ and the electron density $N(x,t)$ respectively. Time between successive vertical display is $2000\Delta t$ where Δt is taken as 0.01 in unit of $\Delta x/V_P$.

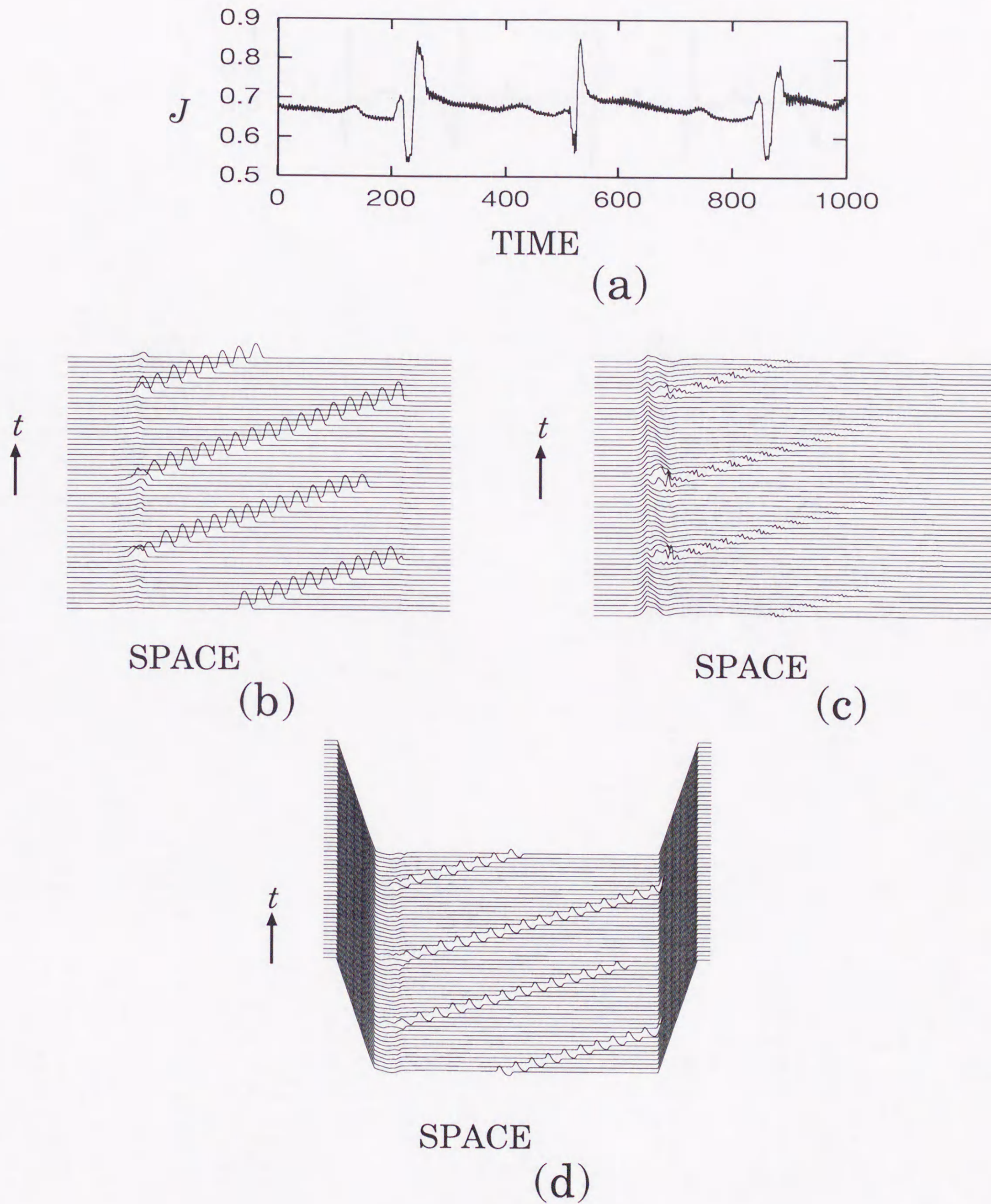

Figure 3.5 The same as Fig. 3.4 for the case Φ_{dc}=12[V] and $\gamma_0 = 1.0 \times 10^{-6}$[cm^3/s] with the impact-ionization effect.

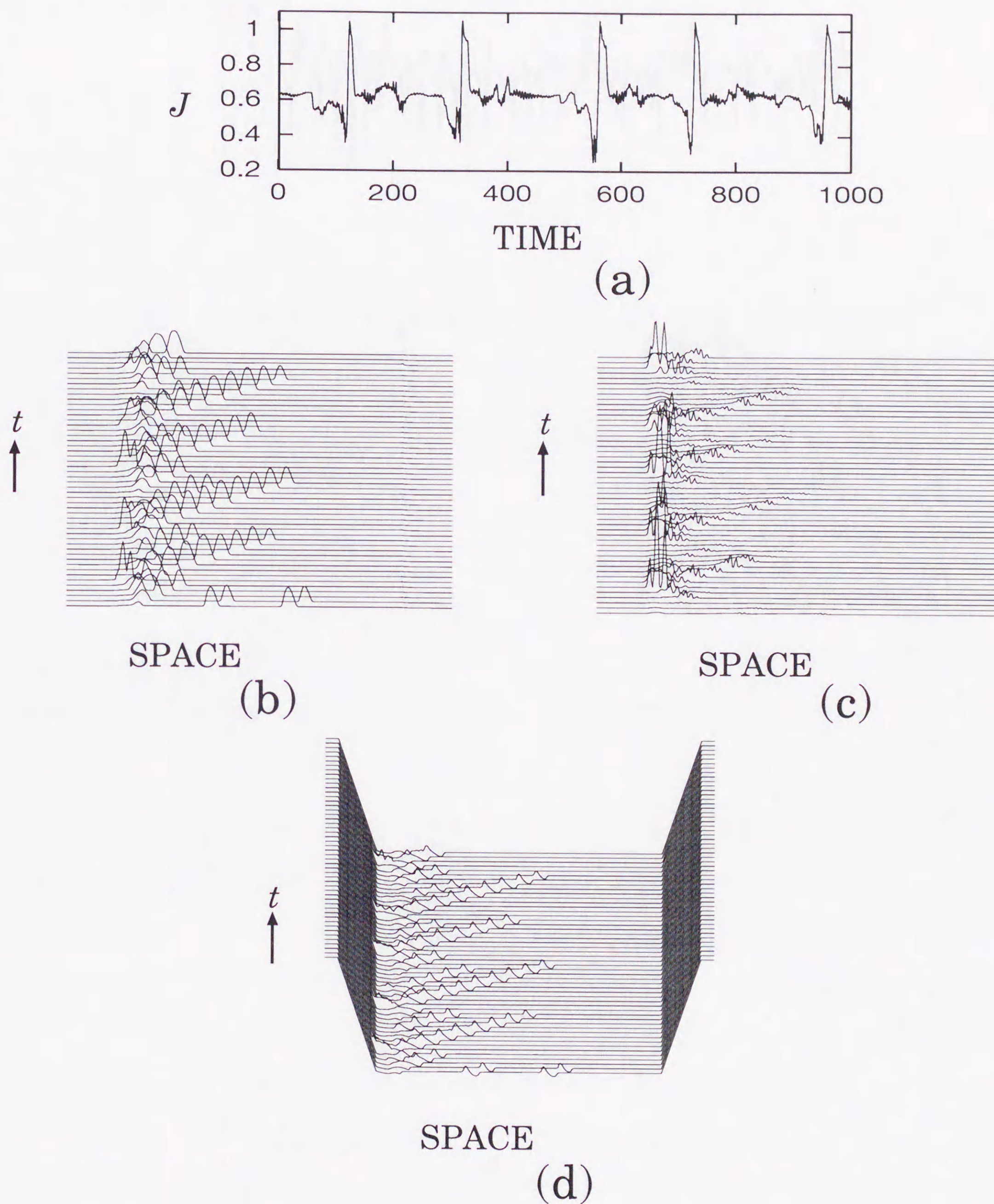

Figure 3.6 The same as Fig. 3.4 for the case Φ_{dc}=20[V] and $\gamma_0 = 1.0 \times 10^{-5}$[cm^3/s] with the impact-ionization effect.

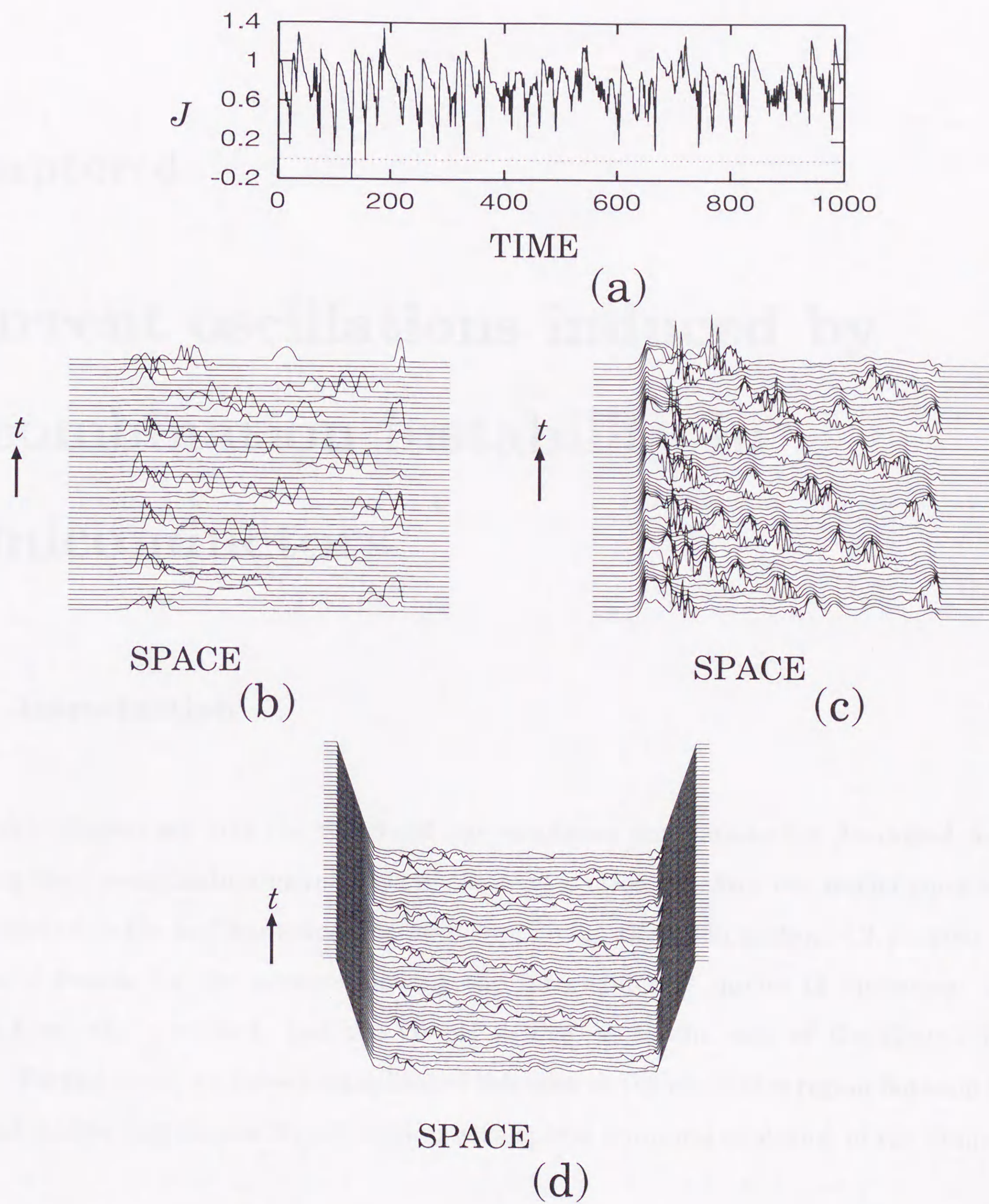

Figure 3.7 The same as Fig. 3.4 for the case Φ_{dc}=20[V] and $\gamma_0 = 1.0 \times 10^{-6}$[cm^3/s] with the impact-ionization effect.

Chapter 4

Current oscillations induced by recombination instability in semiconductors

4.1 Introduction

In this chapter we give the results of our numerical simulations for Au-doped n-Ge showing the recombination instability. In the next section we show our model equations for Au-doped n-Ge and numerical methods for solving them. In section 4.3 we give the numerical results for the system showing the three different modes of operation: the transit-time, the quenched, and the Ohmic modes, as in the case of the Gunn-effect device. Furthermore, we show a complicated behavior in the transition region between the different modes and discuss its connection with spatio-temporal evolution of the domain.

4.2 Equations of motion and simulation method

We consider a one-dimensional system of Au-doped n-Ge. The electric current density

$J(x,t)$ is defined as the sum of the drift term and the diffusion term by

$$J(x,t) = -\,en(x,t)(-\mu)E(x,t) + eD\frac{\partial n(x,t)}{\partial x} \tag{4.1}$$

where $n(x,t)$ is the conduction-electron-carrier density, and $\mu(>0)$ is the electron mobility. The electric potential $\Phi(x,t)$ is defined by

$$E(x,t) = -\,\frac{\partial \Phi(x,t)}{\partial x} \tag{4.2}$$

and the potential and the carrier densities are related by the Poisson equation

$$\frac{\partial^2 \Phi(x,t)}{\partial x^2} = -\,\frac{e}{\epsilon}\left\{N_{\rm d}(x) - n(x,t) - 2[N_{\rm t}(x) - N^-(x,t)] - 3N^-(x,t)\right\} \tag{4.3}$$

where $N_{\rm t}(x)$ is the time-independent total trap density, $N^-(x,t)$ is the triply-negative-charged occupied trap density, and $(N_{\rm t}(x) - N^-(x,t))$ is the doubly-negative-charged unoccupied trap density.

Time evolution of the occupied trap density and the carrier density is governed by the continuity equations

$$\frac{\partial N^-(x,t)}{\partial t} = -\left(\frac{\partial n}{\partial t}\right)_{\rm g} \tag{4.4}$$

$$\frac{\partial n(x,t)}{\partial t} + \frac{\partial}{\partial x}\left(\frac{J(x,t)}{-e}\right) = \left(\frac{\partial n}{\partial t}\right)_{\rm g} \tag{4.5}$$

$$\left(\frac{\partial n}{\partial t}\right)_{\rm g} = -\alpha_{\rm E} n(x,t)\{N_{\rm t}(x) - N^-(x,t)\} + \beta N^-(x,t) \tag{4.6}$$

$$\alpha_{\rm E} = \alpha_0 + \alpha_{\rm M} \exp\left[-\left(\frac{E_{\rm th}}{E(x,t)}\right)^2\right] \tag{4.7}$$

where α_0 and $\alpha_{\rm M}$ are the recombination coefficients, β is the emission coefficient, and $E_{\rm th}$ is the threshold field for recombination.

The continuity equation for the occupied trap density (4.4) does not have the flux term because traps are at a standstill on their sites. In the generation-recombination terms (4.6) which appear in the continuity eqs. (4.4) and (4.5), the first term expresses the recombination process in which conduction electrons are trapped by unoccupied traps, and the second term expresses the emission process (the process reverse to the recombination) in which trapped electrons are liberated from the occupied traps due to a thermal and/or an optical excitation. We assume the recombination coefficient in the form given by eq.(4.7) [77].

We assume the total trap density $N_t(x)$ (the density of the recombination center) to take the following form for the total length L normalized to be 400

$$N_t(x) = \begin{cases} 0 & (0 \le x \le 20) \\ N_d^* \left[\frac{1}{10}(x-20)\right] & (20 < x \le 40) \\ N_d^* \left[2 - 0.8 \sin\left\{\frac{\pi}{20}(x-40)\right\}\right] & (40 < x \le 60) \\ 2N_d^* & (60 < x \le 340) \\ N_d^* \left[2 - \frac{1}{10}(x-340)\right] & (340 < x \le 360) \\ 0 & (360 < x \le 400) \end{cases}$$

where $N_d^* = N_d/5$, N_d denoting the uniform background donor density in the active region ($40< x \le 360$) [Fig. 4.1]. The concaved region ($40< x \le 60$) near the cathode is the doping notch from which domain nucleation and propagation occur. And the donor doping density $N_d(x)$ is assumed to take the following form for the total length L normalized to be 400

$$N_d(x) = \begin{cases} N_d^* \left[1 + n_0\right] & (0 \le x \le 20) \\ N_d^* \left[1 + n_0 + \frac{1}{5}(x-20)\right] & (20 < x \le 40) \\ N_d^* \left[5 + n_0 - 2 \sin\left\{\frac{\pi}{20}(x-40)\right\}\right] & (40 < x \le 60) \\ N_d^* \left[5 + n_0\right] & (60 < x \le 340) \\ N_d^* \left[5 + n_0 - \frac{1}{5}(x-340)\right] & (340 < x \le 360) \\ N_d^* \left[1 + n_0\right] & (360 < x \le 400) \end{cases}$$

where n_0 is the initial value for the conduction electron density [Fig. 4.1].

In this chapter we deal with eqs.(4.1)-(4.7) to determine spatio-temporal evolution of the field variables $n(x,t), N^-(x,t), J(x,t), E(x,t)$, and $\Phi(x,t)$ subject to appropriate initial and boundary conditions.

We discretize the system in the framework of the finite difference method and first divide the one-dimensional system into l partitions. The notations used to express eqs.(4.1)-(4.7) in the non-dimensional form are as follows: the length of the system L, the length of an equally divided partition $\Delta x = L/l$, the unit of the electric field E_0. Using these parameters, the transformations by which eqs.(4.1)-(4.7) are expressed in the non-dimensional form are such that $x \to Lx$, $t \to (L/\mu E_0)t$, $n(x,t) \to N_d^* n(x,t)$, $N^-(x,t) \to N_d^* N^-(x,t)$, $N_d(x) \to N_d^* N_d(x)$, $N_t(x) \to N_d^* N_t(x)$, $E(x,t) \to E_0 E(x,t)$, $\Phi(x,t) \to E_0 L \Phi(x,t)$,

$J(x,t) \to eN_{\rm d}^*\mu E_0 J(x,t)$. The resulting non-dimensional equations are given by

$$J(x,t) = n(x,t)E(x,t) + D^*\frac{\partial n(x,t)}{\partial x} \tag{4.8}$$

$$E(x,t) = -\frac{\partial \Phi(x,t)}{\partial x} \tag{4.9}$$

$$\frac{\partial^2\Phi(x,t)}{\partial x^2} = S^*\{n(x,t) + 2(N_{\rm t}(x) - N^-(x,t)) + 3N^-(x,t) - N_{\rm d}(x)\} \tag{4.10}$$

$$\frac{\partial N^-(x,t)}{\partial t} = -\left(\frac{\partial n}{\partial t}\right)^*_{\rm g} \tag{4.11}$$

$$\frac{\partial n(x,t)}{\partial t} - U^*\frac{\partial J(x,t)}{\partial x} = \left(\frac{\partial n}{\partial t}\right)^*_{\rm g} \tag{4.12}$$

$$\left(\frac{\partial n}{\partial t}\right)^*_{\rm g} = -\alpha_{\rm E}^* n(x,t)\{N_{\rm t}(x) - N^-(x,t)\} + \beta^* N^-(x,t) \tag{4.13}$$

$$\alpha_{\rm E}^* = \alpha_0^* + \alpha_{\rm M}^* \exp\left[-\left(\frac{E_{\rm th}}{E(x,t)}\right)^2\right] \tag{4.14}$$

where the non-dimensional parameters are defined by $S^* = eLN_{\rm d}^*/(\epsilon E_0)$, $D^* = D/(\mu E_0 L)$, $U^* = \tau\mu E_0/L = 1$, $\alpha_0^* = \tau N_{\rm d}^*\alpha_0$, and $\alpha_{\rm M}^* = \tau N_{\rm d}^*\alpha_{\rm M}$.

Substitution of eq.(4.8) into eq.(4.12) gives

$$\frac{\partial n(x,t)}{\partial t} - U^*\frac{\partial(n(x,t)E(x,t))}{\partial x} - U^*D^*\frac{\partial^2 n(x,t)}{\partial x^2} = \left(\frac{\partial n}{\partial t}\right)^*_{\rm g}. \tag{4.15}$$

The governing equations thus become eqs.(4.9)-(4.11) and (4.13)-(4.15). On the spatially discretized system, the variables $n(x,t)$, $N^-(x,t)$, and $\Phi(x,t)$ are defined at both ends of each partition: $i\Delta x(i = 0, 1, \cdots, l)$, while the variables $E(x,t)$ and $J(x,t)$ are defined at the middle points of each partition: $(i - 1/2)\Delta x(i = 1, 2, \cdots, l)$. The time step of the system evolution is denoted by Δt in unit of $\tau = L/(\mu E_0)$ so that the field variables are defined on the time points $k\Delta t(k = 0, 1, 2, \cdots)$. Equations (4.8)-(4.10) are discretized with the aid of the difference procedure which is spatially centered. The resulting form satisfied by the discretized variables whose position and time are designated by the subscript i and the superscript k respectively are found to be

$$J_{i+(1/2)}^k = \frac{n_i^k + n_{i+1}^k}{2}E_{i+(1/2)}^k + D^*\frac{n_{i+1}^k - n_i^k}{\Delta x} \tag{4.16}$$

$$E_{i+(1/2)}^k = -\frac{\Phi_{i+1}^k - \Phi_i^k}{\Delta x} \tag{4.17}$$

$$\frac{\Phi_{i+1}^k - 2\Phi_i^k + \Phi_{i-1}^k}{(\Delta x)^2} = S^*\{n_i^k + 2((N_t)_i - (N^-)_i^k) + 3(N^-)_i^k - (N_d)_i\} \tag{4.18}$$

Equations (4.11)-(4.15) are discretized with the aid of the difference procedure which is spatially centered and temporally semi-implicit.

$$\frac{(N^-)_i^{k+1} - (N^-)_i^k}{\Delta t} = (\alpha_E^*)_i^k n_i^k \{(N_t)_i - (N^-)_i^{k+1}\} - \beta^*(N^-)_i^{k+1} \tag{4.19}$$

$$\frac{n_i^{k+1} - n_i^k}{\Delta t} - U^* \frac{n_{i+1}^{k+1}E_{i+1}^k - n_{i-1}^{k+1}E_{i-1}^k}{2\Delta x} - U^* D^* \frac{n_{i+1}^{k+1} - 2n_i^{k+1} + n_{i-1}^{k+1}}{(\Delta x)^2}$$

$$= -(\alpha_E^*)_i^k n_i^{k+1}\{(N_t)_i - (N^-)_i^{k+1}\} + \beta^*(N^-)_i^{k+1} \tag{4.20}$$

$$(\alpha_E^*)_i^k = \alpha_0^* + \alpha_M^* \exp\left[-\left(\frac{E_{th}}{(E_{i+(1/2)}^k + E_{i-(1/2)}^k)/2}\right)^2\right]. \tag{4.21}$$

The scheme thus consists of successive iterations using eqs.(4.16)-(4.21).

The equations of motion are integrated under the initial conditions

$$n(x,0) = n_0\ ,\ N^-(x,0) = \frac{N_t(x)}{2}\ ,\ \text{and}\ \Phi(x,0) = \frac{x}{l}\Phi \tag{4.22}$$

and the boundary conditions

$$n(0,t) = n(l,t) = n_0\ ,\ N^-(0,t) = N^-(0,0)\ ,\ N^-(l,t) = N^-(l,0)$$

and

$$\Phi(0,t) = 0, \qquad \Phi(l,t) = \Phi \tag{4.23}$$

where Φ is the applied dc bias voltage across the device. The initial conduction electron density n_0 is assumed to have a uniform value. Ignorance of the detail of the n_0 profile will not affect the time evolution of the system because the conduction electron density is much smaller than that of the donor density by a factor of $10^3 - 10^4$ under low excitation [61]. The values of the system parameters which are kept to be fixed during the present computations are $L = 3.16 \times 10^{-3}$[cm], $N_d = 5.0 \times 10^{14}$[cm^{-3}], $n_0 = 1.0 \times 10^{-3}$ (in unit of N_d^*), $\mu = 5.0 \times 10^3$[cm^2/V·sec], $E_0 = 3.16 \times 10$[V/cm], $E_{th} = 1.0 \times 10^2$[V/cm], $\alpha_0 = 2.0 \times 10^{-9}$[cm^3/sec], $\alpha_M = 3.0 \times 10^{-6}$[cm^3/sec], $D = 1.0 \times 10^2$[cm^2/s], and $\epsilon = 16\epsilon_0 = 1.42 \times 10^{-12}$[F/cm]. These are considered to be typical of the usual Au-doped n-Ge [52,56,58,59-62]. The values of the coefficients α_0 and α_M we use in the present computations are larger than those of experimental data by a factor of 10^3, and the choice is largely determined by their possible lower limits above which our numerical procedures

are feasible. In fact, it takes too much computing time to obtain any significant amount of simulational data in case of using the values of α_0 and α_M compatible with those of the experiments. As for the parameters characterizing discretization, the number of the space partition l_n is below assumed to be $l_n = 400$. Under these conditions, the computations were performed to pursue spatio-temporal evolution of the system for several chosen values of the control parameters Φ and β.

4.3 Simulational results

In this section we give the results of our numerical simulations using eqs.(4.16)-(4.21) for a one-dimensional system of Au-doped n-Ge. For suitably chosen values of the model parameters we have found the system becomes electrically unstable and current oscillations appear which are associated with the formation and the cyclic propagation of the domain. Such is a common feature in the systems which have the N-shaped $J-E$ characteristic.

4.3.1 Fundamental motions

We below give several examples of our numerical simulations for the case $\Phi = 0.14$[V]. At low values of β the system exhibits periodic current oscillations associated with a high-field domain cyclically propagating from the cathode to the anode (the transit-time mode). The simulational results at $\beta = 7.56 \times 10^7[\mathrm{sec}^{-1}]$ for this mode are shown in Figs. 4.2(a) and 4.2(b) for time evolution of the total current density at the anode $J(l,t)$ and spatio-temporal evolution of the electric field $E(l,t)$ respectively. A permanent bump of the electric field, *i.e.*, the remaining domain exists persistently over the range of the notch because we have assumed the donor density profile such that it sets up an inhomogeneous field distribution of this form. If the electric field is sufficiently high and the emission coefficient is small so that the recombination between conduction electrons and unoccupied traps predominates, the conduction electrons which flow into the domain are trapped by unoccupied traps. As a result, the electrically negative space charge on

the cathode (or the upstream) side of the domain increases while trapped electrons on the anode (or the downstream) side of the domain are liberated from occupied traps by the excitation and they drift away from the domain due to the voltage imposed on the device to such a degree that the negative space charge on the anode side of the domain decreases. Thus with growth of the remaining domain a large number of the associated conduction electrons become trapped. This process repeats itself and causes the domain to grow larger until the recombination instability balances with the emission and the diffusion. Furthermore, under a sufficiently high bias the grown domain detaches itself from the notch and moves downward towards the anode without changing the shape till reaching the anode. The motion of the domains gives rise to current oscillations. Figures 4.2(a) and 4.2(b) show clearly that the current oscillations are closely associated with the motion of the domains. In this mode we analyzed the dependence of the domain width and the velocity on the voltage imposed on the device. We estimated the velocity of the domain V_{D} from the time during which the leading edge of the traveling domain moves between the space points $x = 0.4$ and $x = 0.7$. The reason why we have chosen these points for measuring the time spent by the passage of the domain is that at $x = 0.4$ the traveling domain has already been matured and that at $x = 0.7$ it has not been affected by non-active region near the anode. Thus the traveling domain moves with the constant velocity and the fixed shape in this region. As for the width, we took the half-valued width as the domain width W_{D} and measured it at the time when the leading edge of the domain reached the point $x = 0.7$. We have found that the width of the domain is proportional to the voltage [Fig. 4.3], and that its velocity is hardly dependent on the voltage [Fig. 4.4], both in accordance with the results observed experimentally [61,63]. However, there are considerable discrepancies of the magnitude of V_{D} and W_{D} between the present and the observed results. We consider these are due to the inappropriate choice of the parameters α_0 and α_M in our computations as mentioned earlier.

At intermediate values of β the traveling domain is quenched before reaching the anode, and the high-frequency current oscillations emerge. Since the recombination causes the domain instability and the value of β represents the rate of the emission which is a reverse process against the recombination, the growth of the traveling domain is curtailed, if β takes a larger value. So the domain cannot sustain its shape and is quenched before

reaching the anode. At the same time, however, the remaining domain begins to grow again. The cycle thus repeats itself (the quenched mode). The simulational results at $\beta = 9.6 \times 10^7$[sec^{-1}] for this mode are shown in Figs. 4.5(a) and 4.5(b).

At higher values of β the system exhibits a steady-state behavior (the Ohmic or steady mode). The simulational results at $\beta = 1.0 \times 10^8$[sec^{-1}] for this mode are shown in Figs. 4.6(a) and 4.6(b). In this mode, at the moment when the domain detaches itself from the remaining domain in the form of a traveling domain, it gets quenched immediately due to the large value of β. Therefore the traveling domain cannot persistently exist.

For the case in which β is fixed, with the increase of the voltage Φ the motion changes its form from the Ohmic to the quenched and then to the transit-time mode. At low values of Φ the domain over the range of the notch cannot grow large enough to detach itself from the remaining domain, so the system exhibits steady-state behavior. At intermediate values of Φ the remaining domain grows larger than that of the former case and the domain detaches itself from the notch as a traveling domain. However the traveling domain does not become sufficiently large and is quenched before reaching the anode. At higher values of Φ the traveling domain grows large enough to reach the anode and the system exhibits an oscillatory behavior whose frequency is determined by the time during which the traveling domain moves from the cathode to the anode. Figure 4.7 shows how appearance of the different mode of motion depends on the voltage Φ and the emission coefficient β. The three modes of operation found in the present system are the same in the case of the Gunn-effect device, as shown in the previous chapters, and the mechanisms giving rise to these can be understood in a similar manner [78].

4.3.2 Peculiar motions

In addition to the above, we have found the change of the periodicity of current oscillations including nonperiodicity in the transition region between the quenched and the transit-time mode. We below show several results of our numerical simulations. At the phase point D (Φ=0.18[V], $\beta = 8.0 \times 10^7$[sec^{-1}]) on the phase diagram Fig. 4.7, the system exhibits current oscillations with the frequency $f_0/2$ as shown in Fig. 4.8. This is to be compared with the results at the phase point G [Fig. 4.11] where the motion exhibits a typical transit-time mode with f_0 being the fundamental frequency for the transit-time

mode (Φ=0.19[V], $\beta = 7.0 \times 10^7$[sec^{-1}]). Figure 4.8(b) shows that traveling far-reaching domains (we call these simply "the main domain" below) reach the anode completely, and traveling sub-domains (we call these simply "the sub domains" below) whose size is much smaller than the main domain appear at every other fixed instant somewhere intermediate between the successive starting times for the main domain near the cathode and they are quenched at certain downstream space point well before reaching the anode. Since the parameter point D in the diagram (Φ,β) is close to the regime for the quenched mode, the growth instability of the remaining domain is almost as strong as that of the traveling domain. In the arguments given below, it is to be noted that the total size (or the total summed area below the $E(x,t)$ curve) of the remaining domain, the main domain, and the sub domain is always constant because the potential imposed over the system is kept fixed. There are cases in which a sub domain:I detaches itself from the remaining domain before the main domain:II reaches the anode and this sub domain:I is subsequently quenched simultaneously with extinction of the main domain:II at the anode. Now that a new main domain:III grows larger than the previous one:II it detaches itself from the remaining domain, and the subsequent sub domain detachment does not occur during the time in which the present main domain:III is propagating. The remaining domain continues to grow large and wide owing to the absence of the sub-domain in the previous stage, as long as the main domain:III propagates gradually diminishing its size. So at this time the large portion of the remaining domain is left as the remaining domain, and the main domain:IV detaches itself with smaller size comparing the last main domain:III. Thus the sub domain:V can now detach itself before the main domain:IV reaches the anode. The cycle thus repeats itself and the oscillations with the double period emerge. In Fig. 4.7 in the phase diagram, the motion is classified as the quenched mode for the case in which any traveling domain never reaches the anode, and as the transit-time mode for the case in which the traveling domain reaches the anode if only once.

At the phase point E (Φ=0.19[V], $\beta = 8.0 \times 10^7$[sec^{-1}]) the system exhibits period 4 (or the frequency $f_0/4$) current oscillations. This is associated with the motion of the domains where the sub domain appears as shown in Figs. 4.9 with the period which is quadruple the one for the main domain, *i.e.*, at every four fixed instants somewhere intermediate between the successive starting times for the main domain at the cathode.

At the phase point F (Φ=0.14[V], β=7.7584$\times$10^7[sec^{-1}]) the system exhibits period 2 current oscillations as shown in Fig. 4.10. The current oscillations with the period 2 are caused by the fact that the vanishing points of the far-reaching traveling domains:I and II are alternately slightly different from each other. Although in this case any domain never reaches the anode, which is different from the case for the phase point D, we consider the mechanism which leads to period 2 oscillations is quite similar to that mentioned above.

Furthermore at the phase point H (Φ=0.14[V], $\beta = 7.636 \times 10^7$[sec^{-1}]) the system exhibits non-periodic current oscillations as shown in Figs. 4.12. Figure 4.12(b) shows that the non-periodic oscillations are caused by stochastic quenching of the traveling domains. In this case, it is impossible to predict the point at which the traveling domain gets extinguished. Figure 4.12(c) is the Lorenz map $|J|_{i+1} = f(|J|_i)$, where $|J|_i$ denotes the value of the ith maximum of the current-density time series. Only the maxima whose values are above 1.1 are plotted, because these are the maxima that are related with stochastic quenching of the main domain. This map also shows clearly the absence of correlation between the values of successive maxima of the current density.

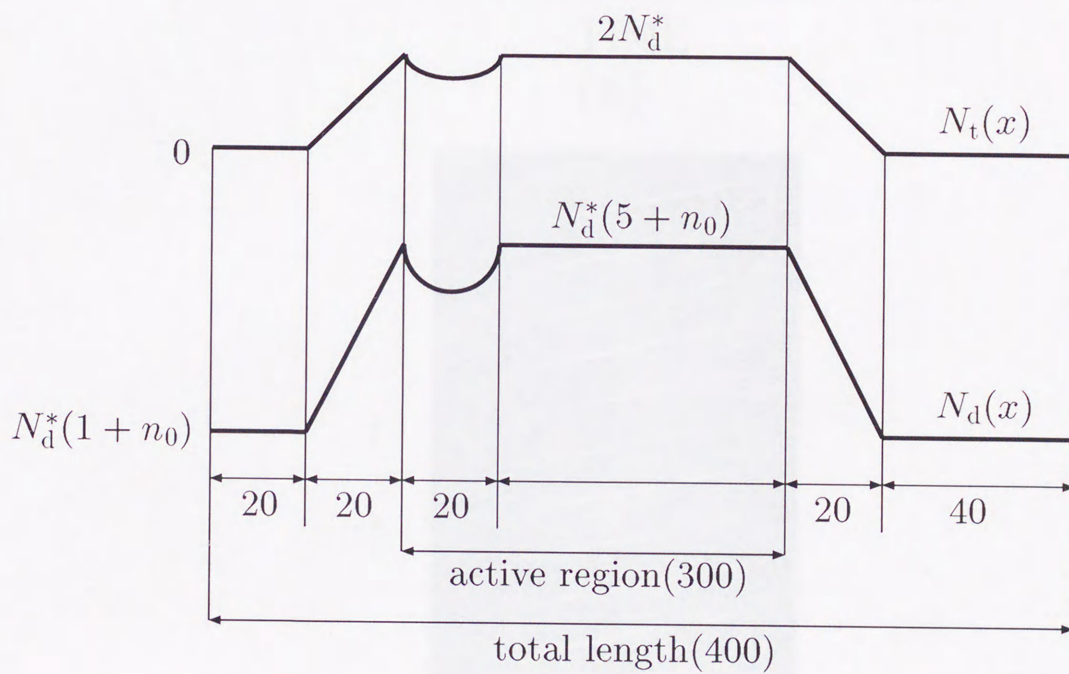

Figure 4.1 The profiles for the total trap density $N_t(x)$ (the upper line) and the donor density $N_d(x)$ (the lower line) where the total length is normalized to be 400.

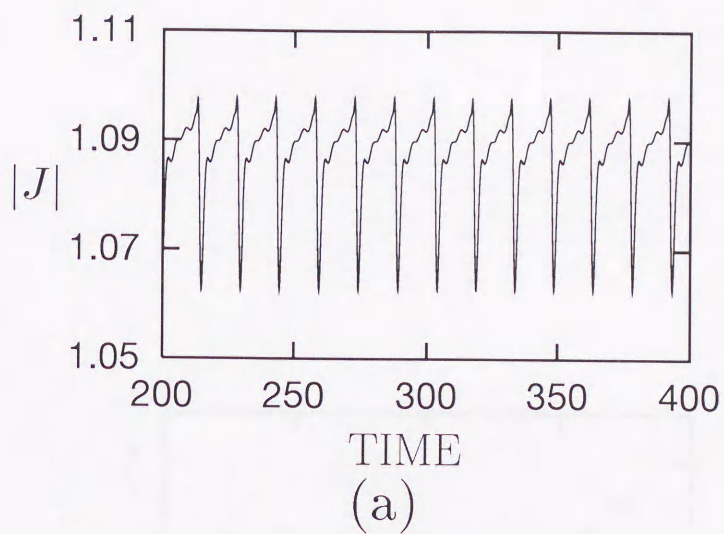

(a)

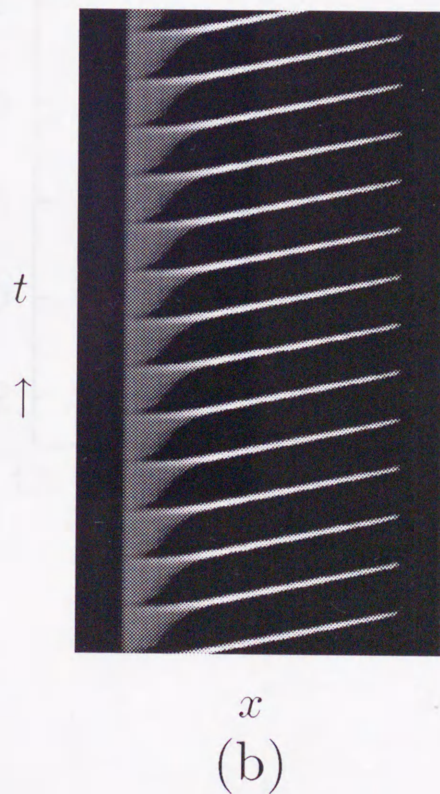

(b)

Figure 4.2 The transit-time mode solution for the case Φ=0.14[V] and $\beta = 7.56 \times 10^7$[sec^{-1}] at the point A in Fig. 4.7. (a)The absolute value of the total current density at the anode $J(l,t)$ [in unit of 2.5 A] as a function of time t [in unit of 2.0×10^{-8} sec]. (b)Spatio-temporal evolution of the electric field $E(x,t)$. The high electric field is represented in such a way that the field intensity increases with the degree of whiteness of the figure.

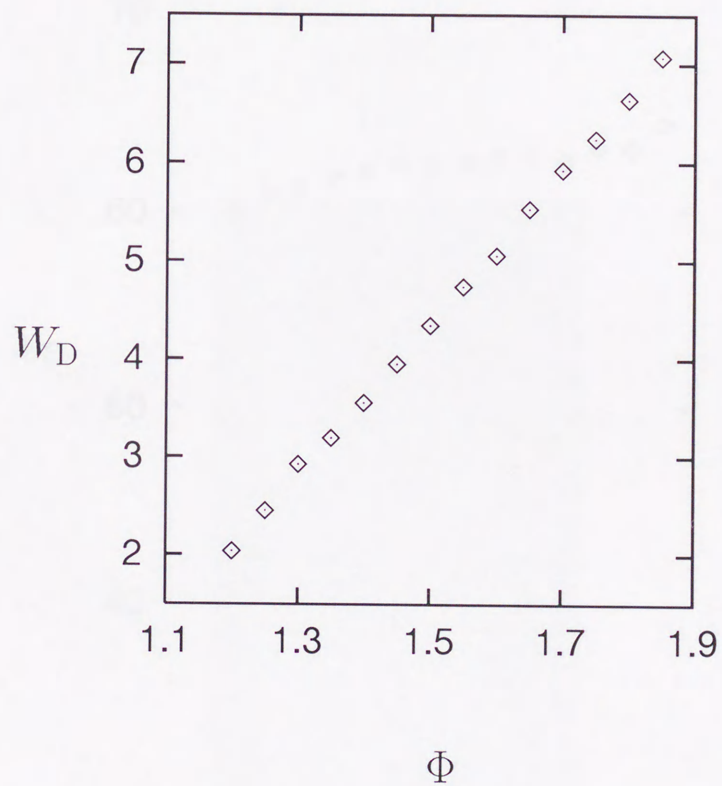

Figure 4.3 Dependence of the domain width W_D [in unit of 10^{-3} mm] on the voltage imposed on the device Φ [in unit of 10^{-1} V].

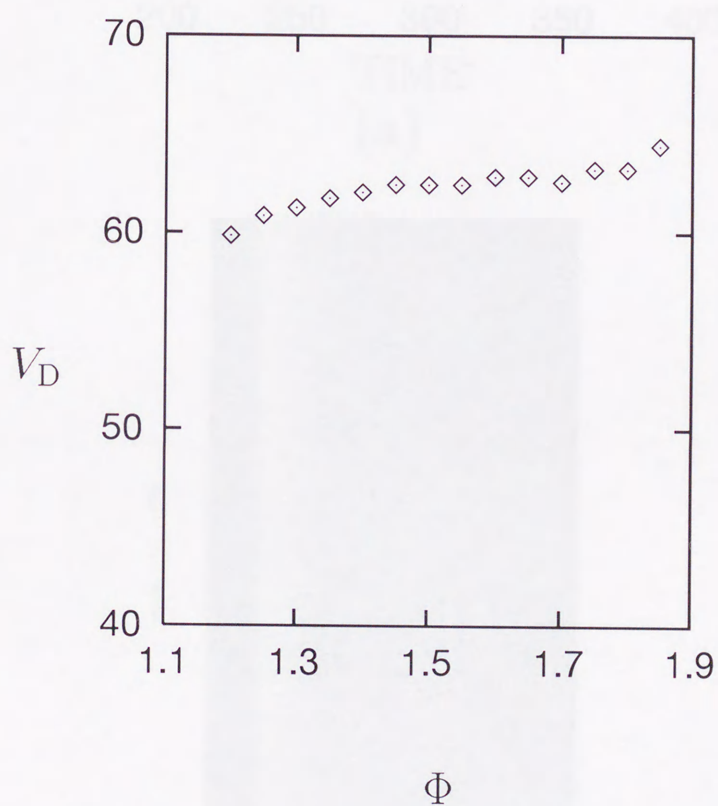

Figure 4.4 Dependence of the domain width V_D [in unit of 10^{-3} mm] on the voltage imposed on the device Φ [in unit of 10^{-1} V].

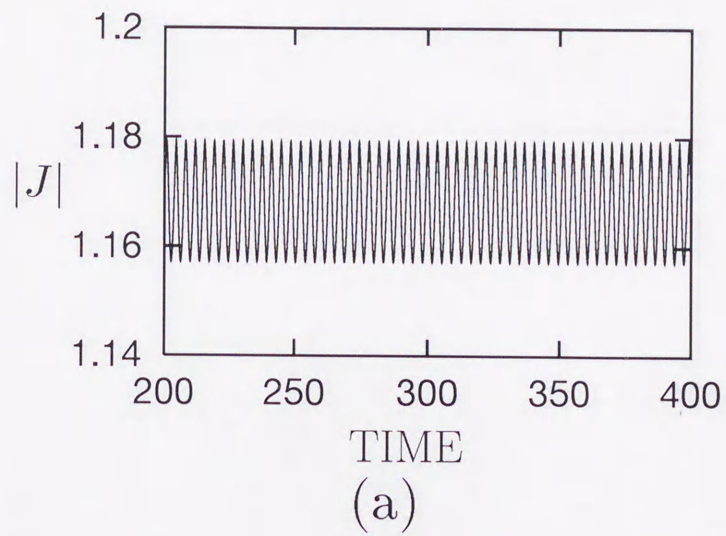

(a)

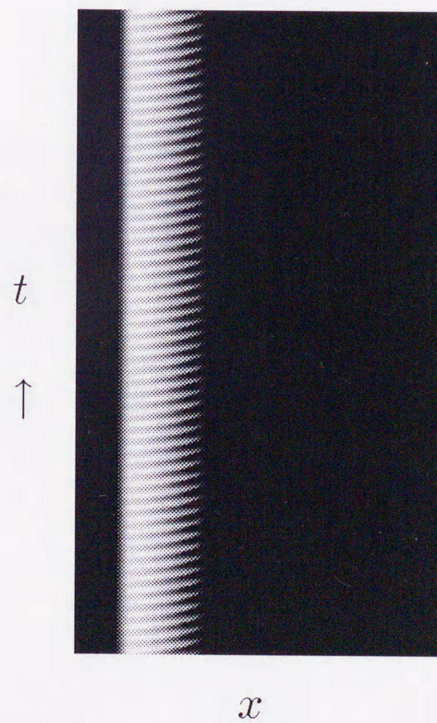

(b)

Figure 4.5 The quenched mode solution for the case Φ=0.14[V] and $\beta = 9.6 \times 10^7$ [sec^{-1}] at the point B in Fig. 4.7 shown in the same way as in Fig. 4.2.

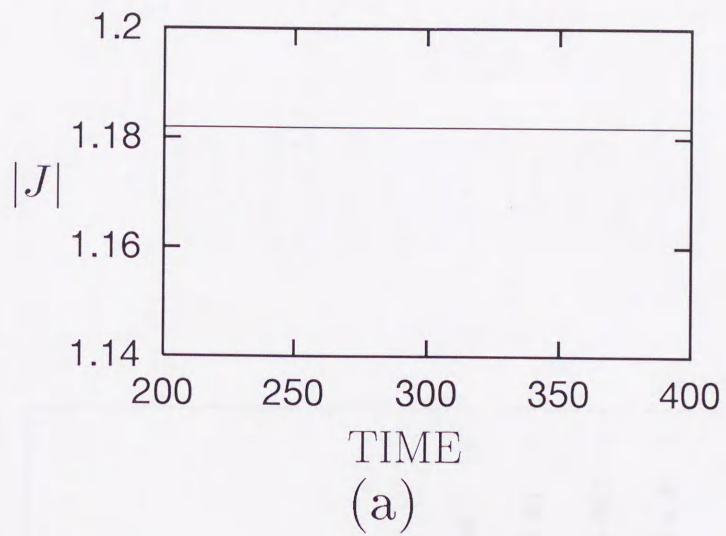

(a)

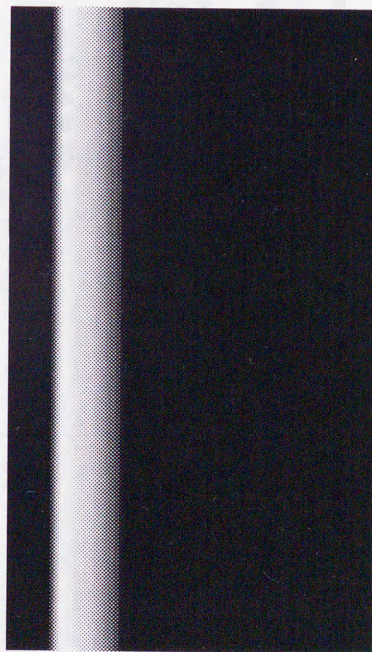

(b)

Figure 4.6 The Ohmic mode solution for the case Φ=0.14[V] and $\beta = 1.0 \times 10^8$[sec^{-1}] at the point C in Fig. 4.7 shown in the same way as in Fig. 4.2.

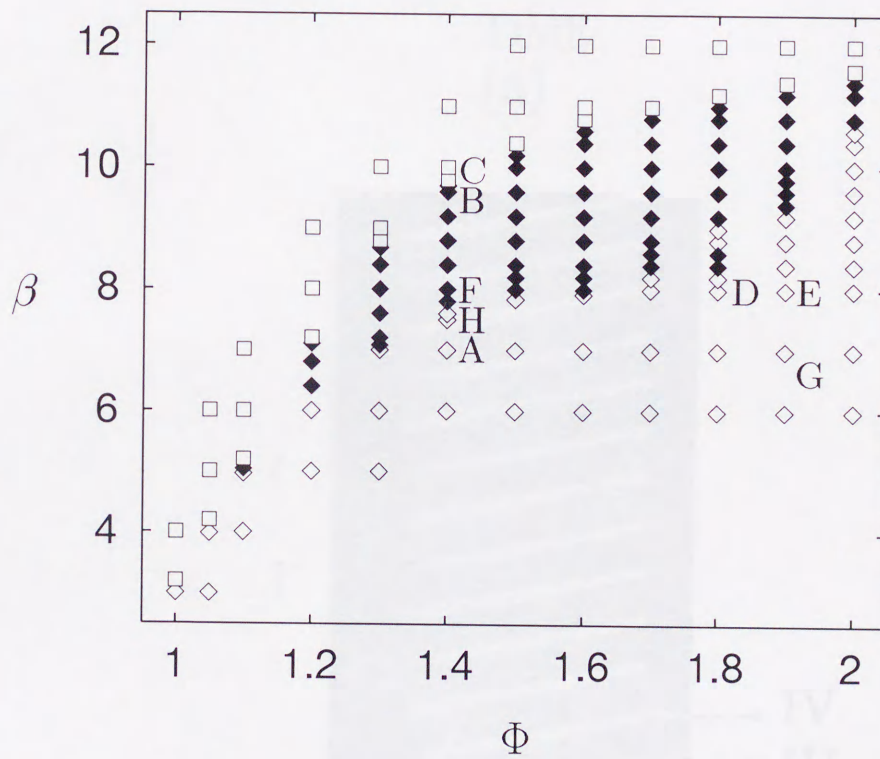

Figure 4.7 The bias voltage $\Phi[\times 10^{-1}\text{V}]$ and the emission coefficient $\beta[\times 10^{7}\text{sec}^{-1}]$ are plotted to show a range of the set of the values in which the Ohmic (open squares), the quenched (solid diamonds) and the transit-time (open diamonds) modes appear.

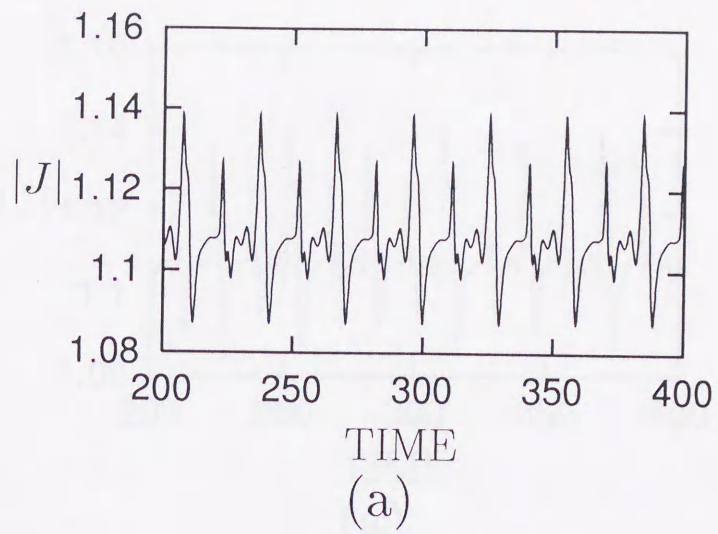

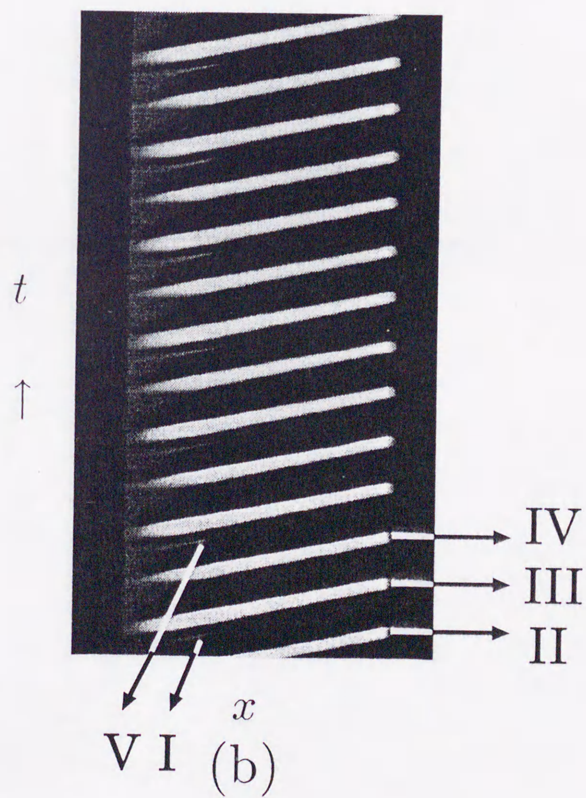

Figure 4.8 The period 2 motion for the case Φ=0.18[V] and $\beta = 8.0 \times 10^7$[sec^{-1}] at the point D in Fig. 4.7 shown in the same way as in Fig. 4.2. In Fig. 4.8(b) the Roman numerals are attached to some domains for a help of the elucidation of the mechanism in section 4.3.

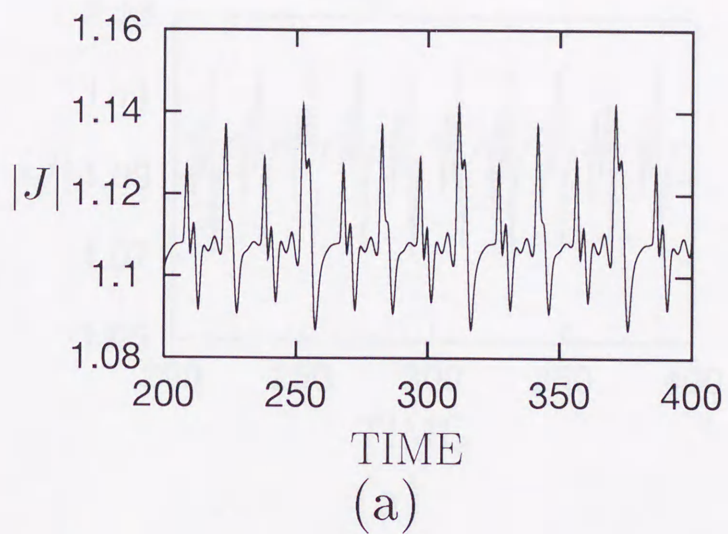

(a)

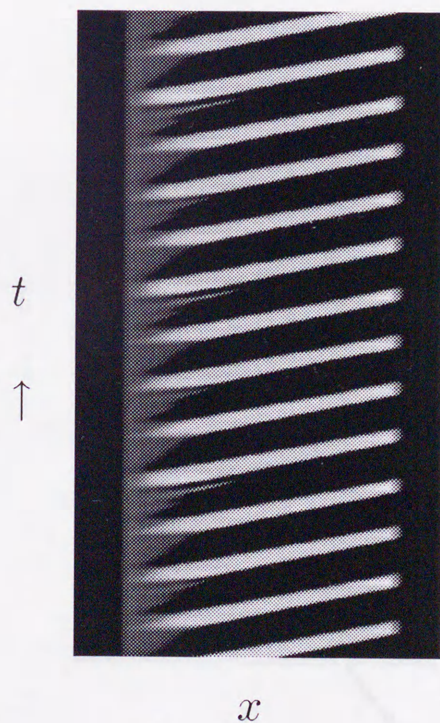

(b)

Figure 4.9 The period 4 motion for the case Φ=0.19[V] and $\beta = 8.0 \times 10^7$[sec^{-1}] at the point E in Fig. 4.7 shown in the same way as in Fig. 4.2.

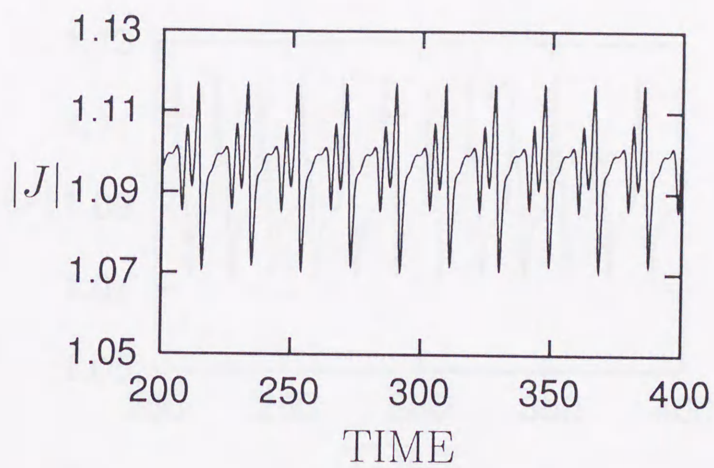

(a)

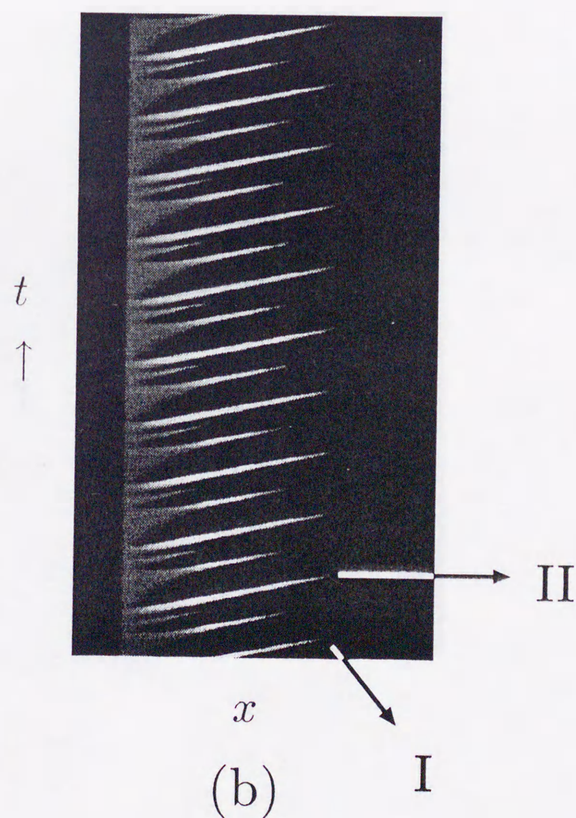

(b)

Figure 4.10 The period 2 motion for the case Φ=0.14[V] and $\beta = 7.7584 \times 10^7$[sec^{-1}] at the point F in Fig. 4.7 shown in the same way as in Fig. 4.8.

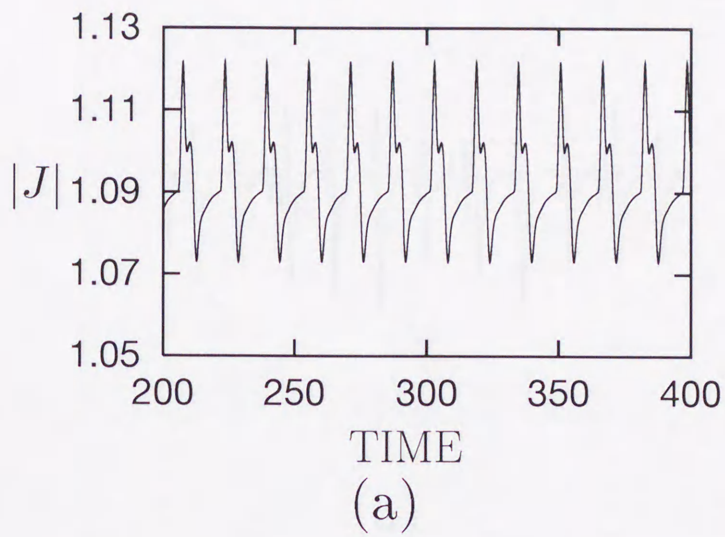

(a)

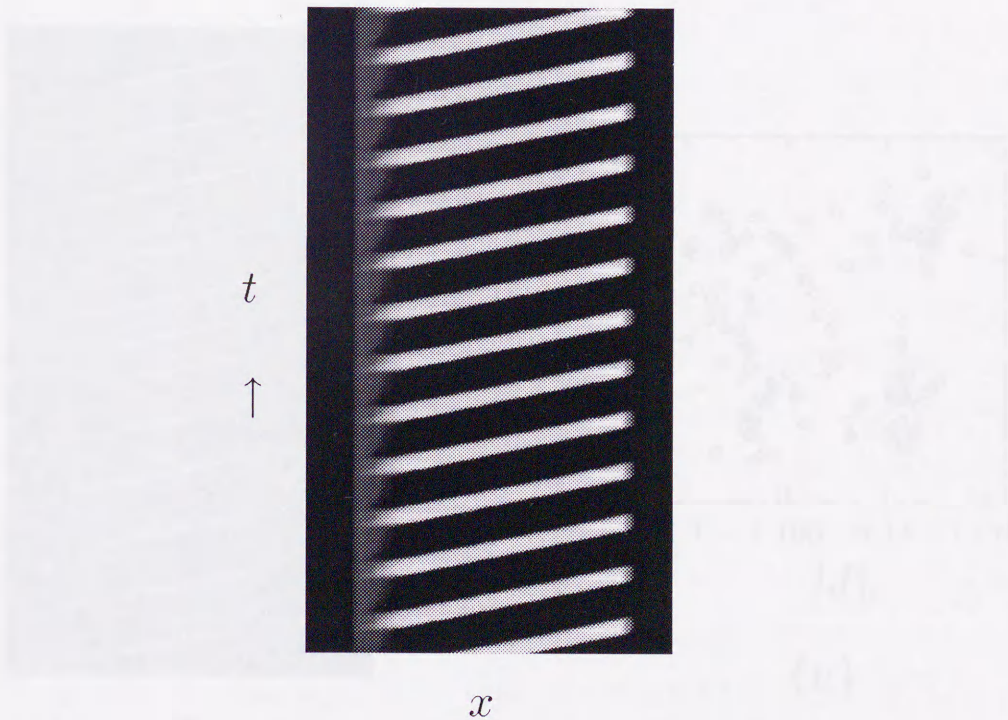

(b)

Figure 4.11 The transit-time mode solution for the case Φ=0.19[V] and $\beta = 7.0 \times 10^7[\mathrm{sec}^{-1}]$ at the point G in Fig. 4.7 shown in the same way as in Fig. 4.2.

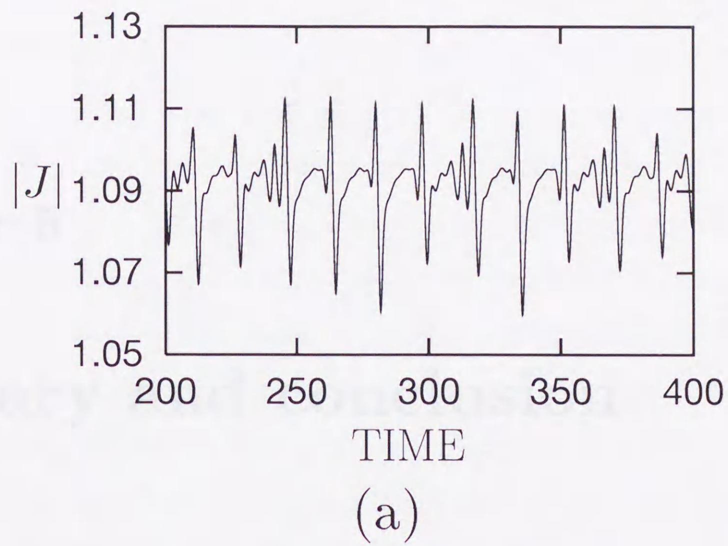

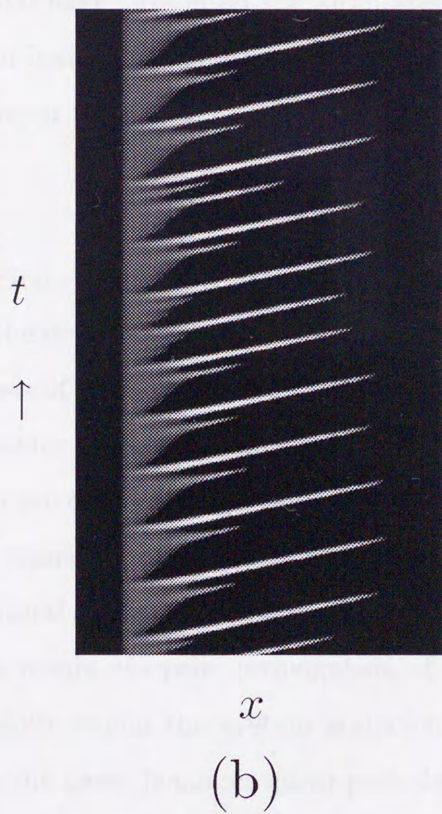

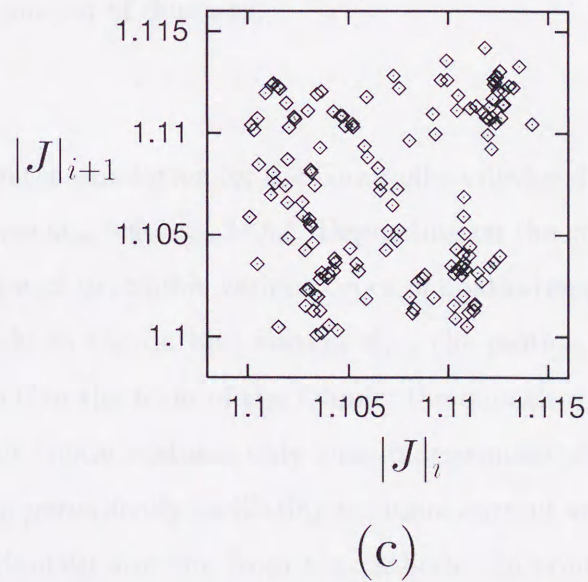

Figure 4.12 The non-periodic motion for the case Φ=0.14[V] and $\beta = 7.636 \times 10^7$[sec^{-1}] at the point H in Fig. 4.7 shown in the same way as in Fig. 4.2, and (c) is the Lorenz map obtained by plotting successive maxima of $|J|(> 1.1)$, $|J|_{i+1} = f(|J|_i)$ during $t = 200 \sim 2000$.

Chapter 5

Summary and conclusion

We have presented the simulational model for semiconductors which exhibit the domain instability, and investigated the dynamics of the system on the basis of the relation between the current oscillations and the motion of domains.

First, we have given the results of computer simulation for the Gunn-effect device driven by the dc and the rf bias voltage of the form $\Phi_{\rm dc} - \Phi_{\rm rf} \cos 2\pi f_0 t$. Depending on the chosen values of $\Phi_{\rm dc}$, $\Phi_{\rm rf}$, and f_0, the system is found to exhibit various types of spatio-temporal behavior. When the device is subject only to the dc bias voltage $\Phi_{\rm dc}$, the motion with increase of its applied value manifests itself in the form of the Ohmic, the quenched, and the transit-time modes. While the Ohmic mode sustains only time-independent steady terminal current, the latter two give rise to periodically oscillating terminal current arising as a result of cyclic propagation of the domain starting from the cathode. In contrast, however, when the system is driven both by the dc and the rf bias voltage, the motion in some cases becomes quasi-periodic and characterized by the subharmonic frequency in addition to the fundamental driving frequency f_0. In particular, we have found that the motion becomes chaotic for specially chosen values of the bias parameters and that the chaotic state is sandwiched between the forward and the reverse period-doubling cascades. At present, it is not clear whether this is experimentally observable. It is difficult to determine the extent to which (i) the present model system adequately describes the experimentally accessible real system and (ii) the present finite difference system gives

a properly approximated solution to the original partial differential equations. We here only make brief comments on the two points, *i.e.*, the numerical integrating scheme and the doping notch which is seemingly most peculiar to the present model system. First, in order to obtain the numerical solutions representing the chaotic motion, we have used a carefully chosen scheme in the sense that in comparison with several other schemes it yields the results with the least amount of the relative errors when the size of Δt is varied over a range from 0.05 to 0.01. Second, in this work, the doping notch is used as a simple model for domain nucleation. Although the quenched mode which is seemingly indispensable to generating chaos is dominated by complicated interactions between the traveling and the remaining domains, it is not clear whether manifestation of chaos critically depends on a special choice of the domain nucleating mechanism.

Next, we have given the results for the Gunn-effect device in which the impact ionization is allowed to occur. For suitably chosen values of the model parameters we have found the interpulse incoherent current oscillations similar to those observed experimentally, and have therein given plausible arguments to the mechanism underlying them on the basis of spatio-temporal evolution of the domain.

Depending on the chosen values of Φ_{dc} and γ_0, the system is found to exhibit complicated spatio-temporal behavior. In this case, the domain motion gets to be more or less perturbed by the resulting carrier generation and recombination. In particular, we have found that the motion becomes non-periodic for specially chosen values of Φ_{dc} and γ_0 even if the rf bias voltage is not imposed. The impact ionization has two main effects on the motion of the Gunn-effect devices as mentioned in section 3.3. First, the holes generated in the traveling domain drift to the cathode and suppress the growth of the remaining domain at the notch region. Second, the carriers(holes and electrons) generated in the traveling domain suppress the growth of the domain itself. So the impact ionization affects both remaining and traveling domains. The motion of the Gunn-effect device is originally governed by the growth competition between the remaining domain at the notch and the detached traveling domain. It is understandable that the motion of the Gunn-effect device thus affected by the impact ionization in an autocatalytic way

exhibits non-periodic behavior under suitably chosen external conditions. In this sense the Gunn-effect device with the impact ionization is one of the dynamical systems which exhibit non-periodic temporal behavior due to their own autonomous nonlinearity even if they are not driven by an external periodic force. However, it is not clear if there exist real n-GaAs systems whose rate of recombination γ_0 is of the same order of magnitude as chosen in our model system. From experimental results available at present [16,32,33,46], we get information on interpulse incoherence only in terms of qualitative description. In order to ascertain whether it occurs in the way similar to that given in chapter 3, it is necessary to get more detailed experimental results on its long-time sustaining conditions and operative recombination processes concomitant with it.

The non-periodic motion occurring in our system exhibits complicated spatio-temporal structure and we have not succeeded in accounting for it in terms of simple deterministic chaos. Nor have we found any bifurcation sequence whereby the domain motion undergoes a transition from periodic to non-periodic behavior.

Third, we have studied the behavior of a one-dimensional system for Au-doped n-Ge. Depending on the chosen values of the model parameters the system is found to exhibit three types of modes of operation which are classified on the basis of spatio-temporal behavior of the system, and spatio-temporal structure of this system develops by the growth competition between the remaining domain at the notch and the detached traveling domains in the same manner as that for the Gunn-effect device. In the transition region between the quenched and the Ohmic modes, no strange behaviors of the system have been observed. On the other hand, in the transition region between the transit-time and the quenched modes we have found the periodicity of the current oscillations undergoes bifurcations and non-periodic oscillations also emerge. Piragas *et al.* reported an experiment on the recombination instability using Cr-doped GaAs where the system exhibits chaotic current oscillations under certain specified conditions, and they tried to clarify the underlying mechanism using a model of ordinary differential equations [68,70]. But their model is not sufficient for describing the system in that the spatial structure of the system such as the formation and the propagation of the domain are not taken into

account at all.

We have found from our computational results that the non-periodic motions occur over a wide range of the parameter space specified by β and Φ. However, we have not succeeded in understanding its complicated spatio-temporal structure in terms of simple deterministic chaos. Furthermore, it is not clear whether the bifurcation routes from periodic to non-periodic oscillations follow the conventional rules commonly observed in simple dynamical systems.

Although we were forced to use the values of the parameters α_0 and α_M which are incompatible with those of real systems, we expect that the results obtained have some validity in predicting the modes of operation occurring in real systems except for the discrepancy of the associated time scales.

As we mentioned before, the motion of semiconductors which have the domain instability under strong excitations is governed by the growth competition between the remaining domain at the notch and detached traveling domains. When an instability of the traveling domain are more dominant than that of the remaining domain, the system exhibits a transit-time mode. For the contrary case the system operates as an Ohmic mode. If an instability of the traveling domain is comparable with that of the remaining domain, a quenched mode emerges. In the systems which are dealt with in this thesis, this quenched mode plays an important role to exhibit peculiar motions. In the case of the periodically-driven Gunn-effect device, an instability of traveling domains is mainly controlled by the time-dependent bias voltage. When the bias voltage is as low as that corresponds to the quenched mode, the instability of traveling domains is weakened, and as the voltage increases the system backs into the regime for the transit-time mode. Thus a subtle balance of the growth competition between domains is realized. It is well known that forced oscillators such as described by Duffing's equation [86] can exhibit chaotic behavior, and its dynamical behavior is described in terms of ordinary differential equations without recourse to the spatial degree of freedom. Semiconductors which have the domain instability are among spatio-temporal oscillators in that current oscillations emerge due to the formation and the cyclic propagation of domains. It is naturally expected that such

spatio-temporal oscillations also exhibit chaotic behaviors as we found in the periodically driven Gunn-Effect device. However, the Gunn-effect device with the impact ionization and Au-doped n-Ge have shown peculiar motions even under a static external field. In such cases, the impact ionization and the emission by excitations suppress the growth of traveling domains, and in the parameter space spanned by the control parameters, the area where a growth rate of traveling domain is comparable with that of the remaining domain is widely expanded. Thus quasi-periodic and chaotic motions have been observed by computer simulations.

In our model the parameters have been chosen mostly from experimental data so that our results are expected to be observed in real systems. Apart from the comparison with the experiments, we have obtained instructive information on the system which is different from that driven under the periodic boundary conditions in that in our case the domains are formed and start traveling at certain specified region of the system. We believe that some common feature can be extracted from the system which has the domain instability associated with various microscopic mechanisms, and further studies on this problem will promote better understanding of nonlinear and non-equilibrium systems.

Bibliography

[1] E.Schöll: *Nonequilibrium Phase Transitions in Semiconductors* (Springer, Berlin, 1987), and the references cited therein.

[2] F.-J.Niedernostheide (Ed.): *Nonlinear Dynamics and Pattern Formation in Semiconductors and Devices* (Springer, Berlin, 1995).

[3] B.K.Ridley: Proc. Phys. Soc. **82** (1963) 954.

[4] V.L.Bonch-Bruevich, I.P.Zvyagin, and A.G.Mironov: *Domain Electrical Instabilities in Semiconductors* (Consultants Bureau, New York, 1975).

[5] H.Krömer: Phys. Rev. **109** (1958) 1856.

[6] B.K.Ridley and T.B.Watkins: Proc. Phys. Soc. **78** (1961) 293.

[7] C.Hilsum: Proc. IRE (1962) 185.

[8] J.B.Gunn: Solid State Comm. **1** (1963) 88.

[9] J.B.Gunn: IBM J. Res. Dev. **8** (1964) 141.

[10] H.Krömer: Proc. IEEE **52** (1964) 1736.

[11] A.R.Hutson, A.Jayaraman, A.G.Coriell, and W.L.Feldman: Phys. Rev. Lett. **14** (1965) 639.

[12] D.E.McCumber and A.G.Chynoweth: IEEE Trans. Electron Devices ED-**13** (1966) 4.

[13] H.Krömer: IEEE Trans. Electron Devices ED-**13** (1966) 27.

[14] H.W.Thim: J. Appl. Phys.,**39** (1968) 3897.

[15] H.L.Grubin, M.P.Shaw, and P.R.Solomon: IEEE Trans. Electron Devices ED-**20** (1973) 63.

[16] P.R.Solomon, M.P.Shaw, H.L.Grubin, and Roger Kaul: IEEE Trans. Electron Devices ED-**22** (1975) 127.

[17] P.R.Solomon, M.P.Shaw, and H.L.Grubin: J.Appl.phys.,**43** (1972) 159.

[18] M.R.Lakshminarayana and L.D.Partain: IEEE Trans. Electron Devices ED-**27** (1980) 546.

[19] G.Goto; T.Nakamura, and T.Isobe: IEEE Trans. Electron Devices ED-**22** (1975) 120.

[20] P.N.Butcher and W.Fawcett: Brit. J. Appl. Phys. **17** (1966) 841.

[21] P.N.Butcher and W.Fawcett: Brit. J. Appl. Phys. **17** (1966) 1425.

[22] H.Krömer: IEEE Trans. Electron Devices ED-**14** (1967) 476.

[23] T.E.Hasty, R.Stratton, and E.L.Jones: J. Appl. Phys. **39** (1968) 4623.

[24] H.Krömer: IEEE Trans. Electron Devices ED-**15** (1968) 819.

[25] R.B.Robrock: IEEE Trans. Electron Devices ED-**16** (1969) 647.

[26] M.Reiser: Electronics Lett.,**7** (1971) 353.

[27] M.Reiser: Comp. Math. Appl. Mech. Engin. **1** (1972) 17.

[28] K.R.Freeman and G.S.Hobson: IEEE Trans. Electron Devices ED-**20** (1973) 891.

[29] K.Yamaguchi, S.Asai, and H.Kodera: IEEE Trans. Electron Devices ED-**23** (1976) 1283.

[30] H.L.Grubin: IEEE Trans. Electron Devices ED-**25** (1978) 511.

[31] H.W.Thim and M.R.Barber: Proc. IEEE Lett. **56** (1968) 110.

[32] J.B.Gunn: IBM J. Res. Dev. **10** (1966) 310.

[33] J.S.Heeks: IEEE Trans. Electron Devices ED-**13** (1966) 68.

[34] C.R.Crowell and V.L.Rideout: Solid State Electronics **12** (1969) 89.

[35] C.R.Crowell and V.L.Rideout: Appl. Phys. Lett. **14** (1969) 85.

[36] V.L.Rideout and C.R.Crowell: Solid State Electronics **13** (1970) 993.

[37] V.L.Rideout: Solid State Electron.,**18** (1975) 541.

[38] A.Zur, T.C.McGill, and D.L.Smith:

[39] J.E.Carrol: *Hot Electron Microwave Generators* (Edward Arnold, London, 1970).

[40] P.J.Balman, G.S.Hobson, and B.S.Taylor: *Transferred Electron Devices* (Academic, New York, 1972).

[41] B.G.Bosch, R.W.H.Engelmann: *Gunn-Effect Electronics* (Wiley, New York, 1975).

[42] S.M.Sze: *Physics of Semiconductor Devices* (Wiley, New York, 1981) 2nd ed..

[43] S. Porowski, W. Paul, J. C. McGroddy, M. I. Nathan, and J. E. Smith: Solid State Comm. **7** (1969) 905.

[44] A. Čenys, G. Lasiene, and K. Pyragas: Solid-State Electron. **35** (1992) 975.

[45] H. Ito, K. Harada and Y. Ueda: Proceedings of 1993 international Symposium on Nonlinear Theory and its Applications **3** (1993) 1015.

[46] M. P. Shaw, H. L. Grubin, and P. R. Solomon: *The Gunn-Hilsum Effect* (Academic, New York, 1979).

[47] H. Gummel and M. Lax: Phys. Rev. **97** (1955) 1469.

[48] V. L. Bonch-Bruevich: Fiz. Tverdogo Tela (Suppl.) (1959) 182.

[49] R. G. Pratt and B. K. Ridley: Proc. Phys. Soc. **81** (1963) 20.

[50] B. K. Ridley and T. B. Watkins: Proc. Phys. Soc. **78** (1961) 710.

[51] B. K. Ridley and R. G. Pratt: Physics Lett. **4** (1963) 300.

[52] R. G. Pratt and B. K. Ridley: Proc. Phys. Soc. **81** (1963) 996.

[53] B. K. Ridley and R. G. Pratt: J. Phys. Chem. Solids **26** (1965) 21.

[54] V. I. Stafeev: Sov. Phys.-Solid State **5** (1964) 2267.

[55] V. L. Bonch-Bruevich and S. G. Kalashnikov: Sov. Phys.-Solid State **7** (1965) 599.

[56] N. G. Zhdanova, M. S. Kagan, and S. G. Kalashnikov: Sov. Phys. -Solid State **8** (1966) 632.

[57] S. G. Kalashnikov, M. S. Kagan, V. A. Vdovenkov: Sov. Phys. -Semicond. **1** (1967) 88.

[58] I. A. Kurova, M. Vrana, and V. S. Vavilov: Sov. Phys. -Solid State. **8** (1967) 1892.

[59] I. A. Kurova and M. Vrana: Sov. Phys. -Semicond. **1** (1968) 917.

[60] M. Vrana, O. A. Kiseleva, and I. A. Kurova: Sov. Phys. -Semicond. **2** (1968) 747.

[61] B. K. Ridley: Proc. Phys. Soc. **86** (1965) 637.

[62] V. L. Bonch-Bruevich: Sov. Phys. -Solid State **8** (1966) 1397.

[63] M. S. Kagan, S. G. Kalashnikov, and N. G. Zhdanova: Phys. Stat. Sol. **24** (1967) 551.

[64] B. K. Ridley and P. H. Wisbey: Brit. J. Appl. Phys. **18** (1967) 761.

[65] See, e.g., H.Haken: *Synergetics, An Introduction*, 3rd ed., Springer Ser. Syn., Vol.1 (Springer, Berlin, Heidelberg, 1983); J.Guckenheimer, P.Holmes: *Nonlinear Oscillations, Dynamical Systems, and Bifurcations of Vector Fields* (Springer, New York, 1983).

[66] K.Aoki and K.Yamamoto: Appl. Phys. **A48** (1989) 111.

[67] K.Nakamura: Prog. Theor. Phys. **57** (1977) 1874.

[68] K. A. Piragas: Sov. Phys.-Semicond. **17** (1983) 652.

[69] S. Bumeliene, J. Požela, and A. Tamaševičius: Phys. Stat. Sol.(b) **134** (1986) K71.

[70] K. Piragas, Yu. Pozhela, A. Tamshyavichyus, and Yu. Ul'bikas: Sov. Phys.-Semicond. **21** (1987) 335.

[71] J. K. Požela, Z. N. Tamaševičiene, A. V. Tamaševičious, J. K. Ulbikas, and G. V. Bandurkina: Phys. Stat. Sol.(a) **110** (1988) 555.

[72] P. A. Maksym and C. J. Hearn: olid State Electronics **21** (1978) 1531.

[73] M. Yamaguchi: *Nonlinear Phenomena and Analysis* (in Japanese), ed. M. Yamaguchi (Nihon-hyoronsha, Tokyo, 1979) p. 13.

[74] E. Mosekilde, R. Feldberg, C. Knudsen, and M. Hindsholm: Phys. Rev. **B41** (1990) 2298.

[75] E. Mosekilde, J. S. Thomsen, C. Knudsen, and R.Feldberg: Physica **D66** (1993) 143.

[76] W. E. Schroeder and G. I. Haddad: Proceedings of the IEEE,**61** (1973) 153.

[77] V. L. Bonch-Bruevich: Sov. Phys. -Solid State **6** (1964) 1615.

[78] K. Oshio and H. Yahata: J. Phys. Soc. Jpn. **62** (1993) 3639.

[79] C. M. Lee, R. J. Lomax, and G. I. Haddad: IEEE Trans. on MTT, MTT-**22** (1974) 160.

[80] C. M. Snowdon: *Introduction to Semiconductor Device Modeling* (World Scientific, Singapore, 1986).

[81] R. Hall and J. H. Leck: Int. J. Electronics **25** (1968) 529.

[82] P. T. Landsberg and A. Pimpale: J. Phys. C **9** (1976) 1243.

[83] P. D. Southgate: J. Appl. Phys. **38** (1967) 4589.

[84] K. Oshio and H. Yahata: J. Phys. Soc. Jpn. **64** (1995) 1823.

[85] Jiang Zongfu and Ma Benkun: Phys. Rev. **B44** (1991) 11072.

[86] Y. Ueda: J. Stat. Phys. **20** (1979) 181.

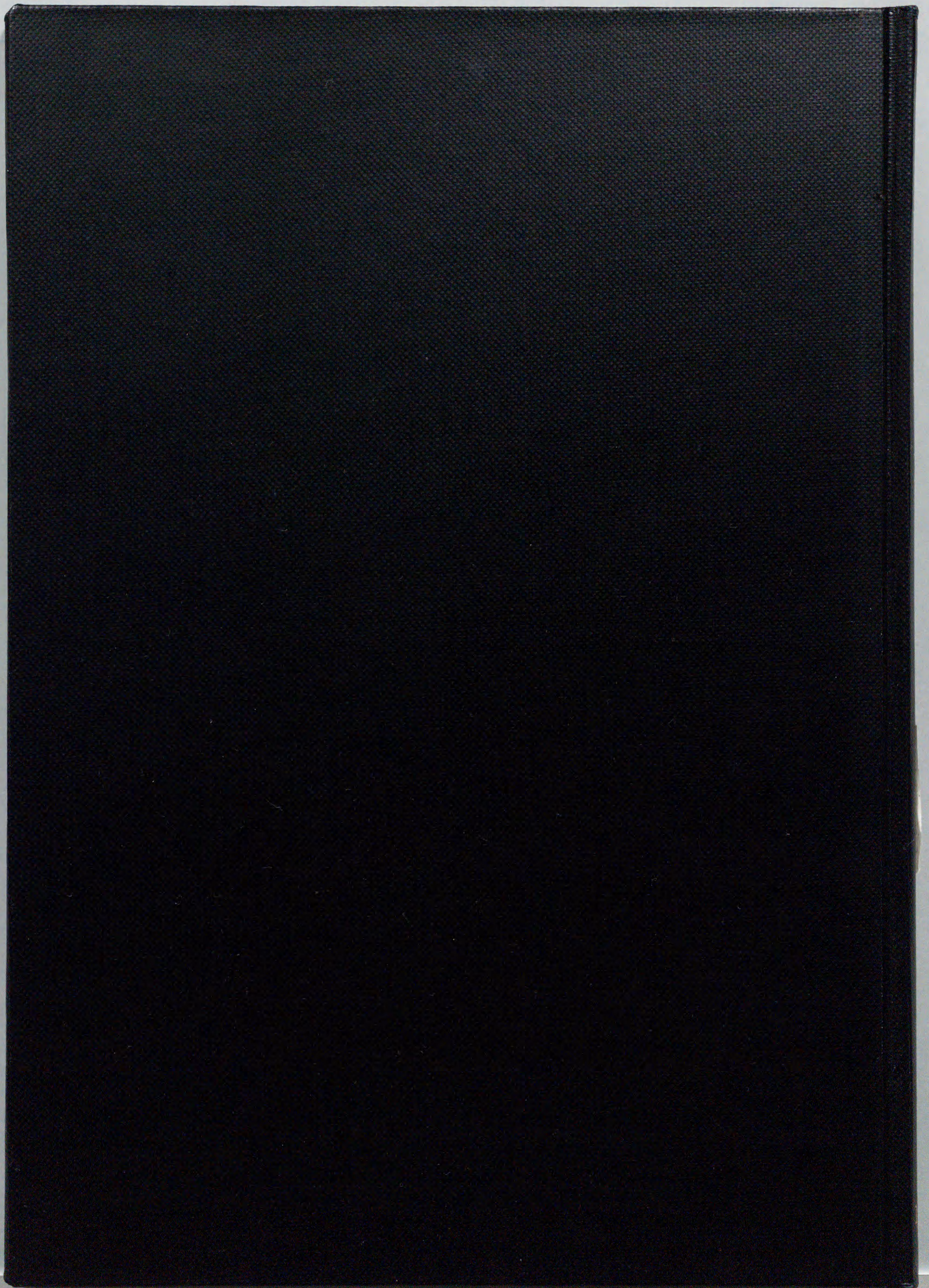

Kodak Color Control Patches

© Kodak, 2007 TM: Kodak

Blue Cyan Green Yellow Red Magenta White 3/Color Black

Kodak Gray Scale

© Kodak, 2007 TM: Kodak

A 1 2 3 4 5 6 M 8 9 10 11 12 13 14 15 B 17 18 19